FACULTY OF SCIENCE
UNIVERSITY OF COPENHAGEN

Jens Tarp

Enforced Scale Selection in Field Theories of Mechanical and Biological Systems

Ph.D. Thesis
September 2015

Enforced Scale Selection in Field Theories of Mechanical and Biological Systems

Prepared by

Jens Tarp

Academic advisors

Joachim Mathiesen

Biocomplexity Group
Niels Bohr Institute
University of Copenhagen
Blegdamsvej 17
DK-2100 København Ø
Denmark

www.nbi.ku.dk

Abstract

The collective motion of driven or self-propelled interacting units is in many natural systems known to produce complex patterns. This thesis considers two continuum field theories commonly used in describing pattern formation and dynamics: The first one, the phase field crystal model, which describes the dynamical and equilibrium properties of crystalline material, is used to study the coarsening dynamics of polycrystalline materials in two and three dimensions. A generalization introducing a faster elastic relaxation time scale is then used to study the plastic deformation and dislocation dynamics of single crystals. Secondly, a continuum theory describing mesoscopic turbulence of biological active matter, which is used to study long-range ordered vorticity patterns generated by cell divisions in a endothelial cell layer.

Publications

1. Mathias Bjerre, Jens M. Tarp, Luiza Angheluta and Joachim Mathiesen

   Rotation-induced grain growth and stagnation in phase-field crystal models

   Physical Review E 88, 020401(R) (2013).

2. Ninna S. Rossen, Jens M. Tarp, Joachim Mathiesen, Mogens H. Jensen and Lene B. Oddershede

   Long-range ordered vorticity patterns in living tissue induced by cell division

   Nature Communications, 5, (2014)

3. Jens M. Tarp, Luiza Angheluta, Joachim Mathiesen and Nigel Goldenfeld

   Intermittent dislocation density fluctuations in crystal plasticity from a phase-field crystal model

   Physical Review Letters, 113(26), 265503 (2014)

4. Jens M. Tarp and Joachim Mathiesen

   Rotation-limited growth of three-dimensional body-centered-cubic crystals

   Physical Review E 92, 012409 (2015)

Contents

CHAPTER 1

Introduction

Throughout nature there exists countless physical systems which experience a transition from random or uniform motion to a state described by the collective motion or collective assembly, generating large-scale patterns in both time and space. The scales describing these patterns can be many orders of magnitude larger than the local length and time scales of the system and often play an important role in determining both equilibrium states as well as non-equilibrium dynamics.

These system span a wide variety of physical phenomena at different spatial and temporal scales from inert metals and dynamics of biological cell layers to flame fronts and flocking of birds. Even so, these systems have several essential features in common. In all of them a larger number of smaller "particles" try to follow their neighbours through time and space and the interaction between the particles is short range, meaning that there is no global "ordering field". The resulting large-scale patterns are an emergent phenomenon from the microscopic system.

Describing these types of systems mathematically can be challenging, since the large-scale structures are not immediately apparent in the microscopic formulation of the problem. In this context "microscopic" is used to denote the description of a system by the building blocks of the problem, which could be birds in a flocking model or cells in cell layer dynamics. It is therefore often necessary to reformulate the problem from a microscopic to a mesoscopic point of view, in order to efficiently study these systems at the length and time scales of the large-scale pattern formation. This simplification process requires careful considerations and it is rarely obvious how the mesoscopic equations should look like. Efficient modelling can become difficult, if too much of the microscopic information is kept within the mesoscopic framework. Conversely, if to little information is kept, detailed information regarding the pattern formation may be lost. In the case of flocking of birds the pattern evolution can adequately be described by a set of equations for the concentration of birds instead of the individual birds [3], while for

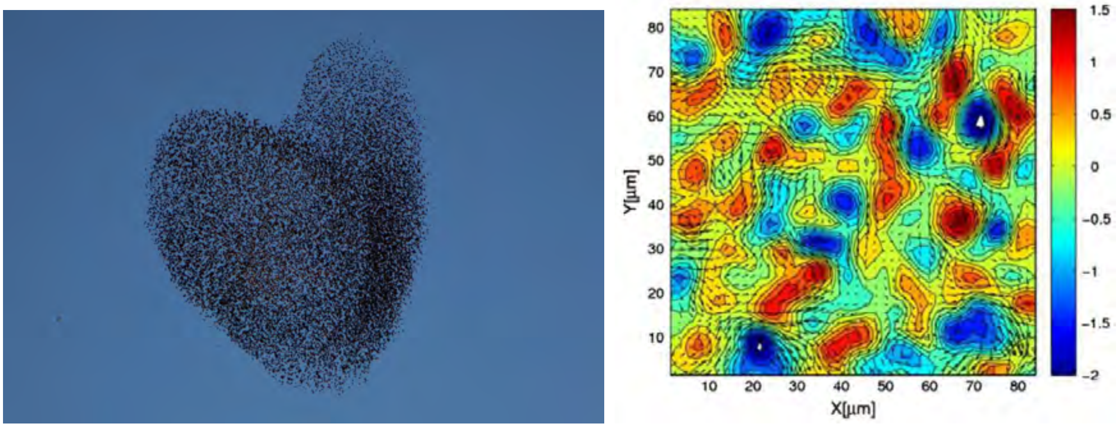

(a) A flock of birds [1].

(b) The vorticity field of swimming *Bacillus subtilis* [2]. The colorbar indicates the magnitude of the vorticity in s^{-1}.

Figure 1.1: Examples of systems showing a characteristic length scale.

cell dynamics the discrete motion of cells can sometimes be satisfactorily described by a set of continuum equations for a whole sheet of cells [4, 5]. It is also a question of what features of the microscopic system should stay intact in the mesoscopic model. In the case of a solidification process it is important to realise whether the interesting questions are about the large-scale dendritic structures or the emergence of anisotropic surface patterns due to the inherent lattice structures of the metal.

In other cases the physical phenomenon is not well enough understood to allow for an accurate microscopic description. In these cases it can be necessary to start at the phenomenological level and directly state mesoscopic equations, which are assumed to capture the correct physics. While this method seems ad-hoc, there are some guidelines which should be followed in order write down a set of physical equations.

In general the microscopic equations governing the pattern formation are often complex non-linear partial differential equations for which the amount of information that can be extracted often is quite limited. One method to describe pattern formations is to assume that the transition from a disordered or uniform state to an ordered state can be described by an order parameter [6]. Assuming the system becomes unstable when the order parameter reaches some critical value $K = K_c$, perturbations with frequency ω_0 and wavevector q_0 will start to grow. For $q_0 \neq 0$ the system exhibits spatial patterns while $\omega_0 \neq 0$ will give oscillatory patterns. In these cases information about the pattern evolution can be derived by expanding the microscopic equations around the transition point and looking at the long time limit. This thesis will mainly be concerned with the case where $q_0 \neq 0$ and $\omega_0 = 0$. In this case the instabilities are periodic in space and stationary in time. In the simplest case with only one dominant mode, this instability describes a roll pattern in two dimensions and planes in three dimensions. By superimposing elementary rolls, more complex lattice structures in two dimensions and three dimensions can be formed such as hexagonal and face-centered-cubic lattices [7].

A classical example of a system which can be analysed in this way is the onset of convection rolls in Rayleigh-Bénard convection in which a fluid is trapped between a hot and a cold plate [8]. The governing equation is known as the Oberbeck-Boussinesq, which is a Navier-Stokes equation with a buoyancy force added due to gravitational acceleration and thermal expansion coupled to a heat diffusion equation. For sufficiently low temperatures the liquid is stationary with a linear temperature gradient from bottom to top. At a critical temperature the heat diffusion is no longer powerful enough to stabilize the system and convection patterns in the fluid velocity develop as well as patterns on the fluid surface called Rayleigh-Bénard cells. In order to describe the evolution of the patterns, Swift and Hohenberg expanded the Oberbeck-Boussinesq equation around a stationary flow resulting in an eigenvalue equation. For a specific set of material parameters and a critical temperature difference of the plates, the eigenvectors of the system split into a fast and a slow eigenvector, with the slow one corresponding to the pattern formation with its governing equation given by

$$\frac{\partial \phi}{\partial t} = \epsilon \phi - \left(q_0^2 + \nabla^2 \right)^2 \phi + \text{N-L}, \tag{1.1}$$

where ϵ is dependent on the temperature difference between the hot and the cold plate and triggers the transition from uniform to a periodic state, q_0 is dependent on the spatial size of the system and determines the equilibrium wavelength of the periodic solution and N-L is some non-linear term left over from the microscopic equations. For $\epsilon > 0$ the uniform phase becomes dynamically unstable and a periodic state emerges as shown in fig 1.2a. For a simple cubic non-linearity, $-\phi^3$, the equilibrium pattern will be stripes in two dimensions. In two, and higher dimensions, the patterns can become unstable to wavelength perturbations as well, resulting in an Eckhaus instability adding to the complex dynamics of the equation [9]. The Swift-Hohenberg equation has been widely studied due to its simplicity and for its pattern formation qualities. Furthermore, its complex generalization can be used to study lasers with a negative detuning [10], while its generalization to curved space recently has found use in describing buckling and folding in biological tissue as well as structure formation in thin films [11].

In the case of simple non-linear terms the equations of motion can be described on variational form, $\partial_t \phi = -\delta \mathcal{F}[\phi] / \delta \phi$, where $\mathcal{F}$ is an effective free-energy describing the equilibrium properties of the system. Using the classification scheme of Hohenberg and Halperin [12], the Swift-Hohenberg equation falls into the model-A type of equations, meaning the order parameter ϕ is not a conserved quantity during evolution. The model described by the Swift-

Hohenberg free energy and model-B conservative dynamics, $\partial_t \phi = \nabla^2 \delta \mathcal{F}[\phi]/\delta\phi$, is called the phase field crystal model and is used to study crystals and their evolution as well as elastic and plastic deformations [13].

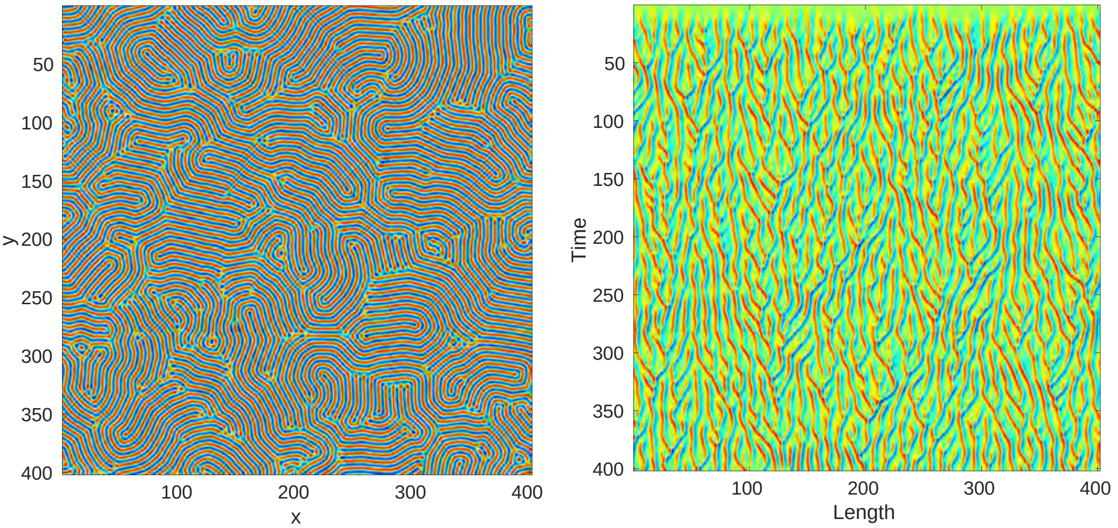

(a) Snapshot from a two-dimensional simulation of the Swift-Hohenberg equation (1.1) with a cubic non-linearity. The colours correspond to the magnitude of ϕ. The system is evolving slowly with the evolution of ordered domains following a power law.

(b) Time evolution of the one-dimensional Kuramoto-Sivashinsky equation. The colors correspond to the magnitude of u. The temporal dynamics shows a chaotic behaviour.

Figure 1.2: A snapshot of (1.1) and time evolution of (1.2).

In a similar fashion to the method outlined above, a broad class of coupled reaction-diffusion equations can be analysed and their pattern equations derived [14]. In common with the Swift-Hohenberg equation, these equations have slow eigenvectors that are described by a high-order partial differential equation working on time scales longer than the original microscopic system.

A perhaps even more famous example of a pattern equation is the Kuramoto-Sivashinsky equation from the mid-1970s, which was among others derived by Kuramoto and Tsuzuki when studying a reaction-diffusion equation [15] and Sivashinsky and co-workers in the study of the evolution of laminar flame fronts [16]. The equation has also found its use in the asymptotic behaviour of two phase flow in pipes [17] as well as models of ion-sputtered surfaces [18]. In one dimension the equation is given by

$$\frac{\partial u}{\partial t} = -\left(\frac{\partial^4}{\partial x^4} + \frac{\partial^2}{\partial x^2}\right) u - u\frac{\partial u}{\partial x}. \tag{1.2}$$

The Kuramoto-Sivashinksy equation has attracted a lot of attention both due to its diverse use, but also since it is one of the simplest non-linear differential equations showing complex spatial and temporal dynamics as shown in fig 1.2b. There has been a large amount of both analytical [19] as well as numerical [20] studies of the one dimensional equation.

The pattern-forming properties of the Swift-Hohenberg equation (1.1) and the Kuramoto-Sivashinsky equation (1.2) can be better understood by plotting the dispersion relation of the linear part of the equations. As shown in fig 1.3a, both curves have a non-zero maximum corresponding to the maximally unstable wavelength, which for long time scales will be the dominant wave length of the system. This is either the wavelength of the rolls or a typical wavelength the system will fluctuate around. Generally, if the linear dispersion relation for a model has a non-zero maxima, the equations will tend to generate solutions with a well-defined length scale. The stability of the solutions is, however, highly dependent on the non-linearity in the equations. In fig 1.3b the magnitudes of the Fourier transforms for the numerical solutions of eq. (1.1) and eq. (1.2) are plotted, showing the large difference in the time evolution between the two equations due to the difference in the non-linearity.

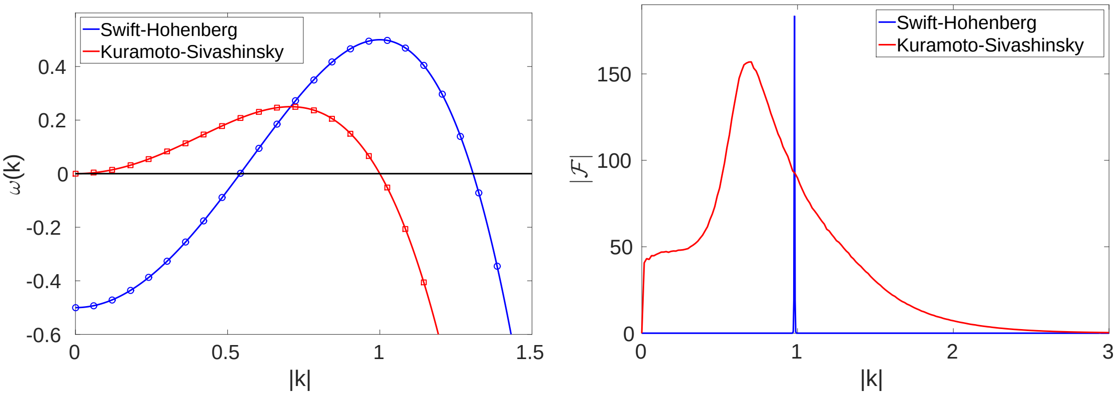

(a) The linear dispersion relation for (1.1) and (1.2). The non-zero maximum in the dispersion relation induces a length scale in the solutions of the equations.

(b) The magnitude of the Fourier transform of the numerical solution of equation (1.1) and the time averaged Fourier transform of (1.2). For the relaxational dynamics of (1.1) the spectrum will slowly evolve towards a delta-function like shape. For the chaotic dynamics of (1.2) the spectrum will retain its width.

Figure 1.3: Dispersion and equilibrium properties of (1.1) and (1.2).

The non-zero maximum in the spectrum is also the starting point for a more pragmatic approach of Brazovskii [21], who argues that as long as the system has a non-zero maxima in its fluctuation spectrum, it is mathematically allowed to expand the dynamics around the maximum in momentum-space in order to derive the equations of motion. These ideas have recently been used to derive phenomenological hydrodynamic models for cell layer motion [4, 5], where the typical Navier-Stokes type of dissipation operator has been replaced by a higher order differential operator inducing a typical length scale to the system mimicking the cell scale.

An implicit assumption in the method above is that boundary effects of a finite system can be neglected as small perturbations. When performing the expansion around the transition point it is assumed that the system can be described by a spatially infinite uniform state. This is not a valid assumption in the class of problems described by moving boundary equations such as dendritic crystallization [22], viscous fingering in a Hele-Shaw cell [23] and phase separation in a binary fluid [24]. In these cases the pattern formation is driven by the boundary conditions between two different phases of matter and can not be neglected.

Some of these problems involve far from equilibrium diffusional limited dynamics and are modelled directly at the mesoscopic level with a diffusion equation in the bulk phase supplemented with flux and transport boundary equations at the interface between the phases. In order to include a length scale into the equations, the transport boundary conditions usually have a Gibbs-Thomson relation between the different phases at the boundary and the curvature of the boundary layer [25]. To find the temporal evolution of a characteristic length scale it is necessary to solve the full equation with boundary conditions, which can be a considerable challenge.

In order to simplify the problems it was found that a wide class of phase field models with dynamics described by model-A, B and C type equations of motion [12], could be shown to follow the same dynamical equations as the moving boundary problems over large time scales [26]. A large part of phase field models can be put into variational forms making it simpler to derive asymptotic estimates [27]. Typical features of these models are that pattern formation is at the boundary of well defined spatial regions, which is in contrast to the patterns observed in the Swift-Hohenberg type equations.

In the phase field approach the moving boundary problem is reformulated as a set of partial differential equations for the phase field. In practice, the phase field models smear out the otherwise sharp interface over a finite region. The entire structure of the system can then be continuously represented by the new field, with distinct values in the different bulk phases and an interpolating region mimicking the interface [28]. This greatly reduces the computational complexity and allows for other analytical methods when studying solutions to the moving boundary problems. In this way phase field models have played an important part in quantifying solutions to classical moving boundary problems.

Chapter 2

Phase Field Crystal Model

The phase field crystal model is a continuum field theory used in modelling of the dynamics and equilibrium properties of crystals. It was developed in order to study the macroscopic properties due to complex microstructures in polycrystals formed during non-equilibrium processes [29]. It exploits the fact that some crystal properties are completely determined by the symmetry of the lattice, such as the type and movement of dislocations and the symmetry of the elastic coefficients. Due to the equilibrium properties of the field, it naturally describes a polycrystal composed of grains with different sizes, shapes and coordination, which can be important parameters for macroscopic properties of materials. The model is based on an atomistic free energy functional while the equation of motion is described by conservative model-B dynamics. This couples the small length-scale of the atomistic free energy with long diffusional time-scales, making it an efficient model for studying complex polycrystalline structures and their evolution.

The model can be considered as a generalization of phase field models of nonequilibrium phenomena such as spinodal decomposition. Often these types of systems can be described by spatially uniform fields with a rapidly changing interface showing a complex morphology. The phase field model for spinodal decomposition can be described by a free-energy functional and model-B type dynamics given by

$$\mathcal{F} = \int dV \left(f(\phi) + \frac{K}{2} |\nabla \phi|^2 \right) \tag{2.1}$$

$$\frac{\partial \phi}{\partial t} = \Gamma \nabla^2 \frac{\delta \mathcal{F}}{\delta \phi}, \tag{2.2}$$

where ϕ is a concentration field and $f(\phi)$ is the bulk free-energy, usually chosen to be a double-well potential. The gradient term will lead to a surface tension which will split the system into smaller domains separated with domain walls and Γ is a phenomenological diffusion constant. This set of equations is also known as the Cahn-Hilliard equations [24] and the model is based on the assumption that the bulk regions should be translationally and rotationally invariant,

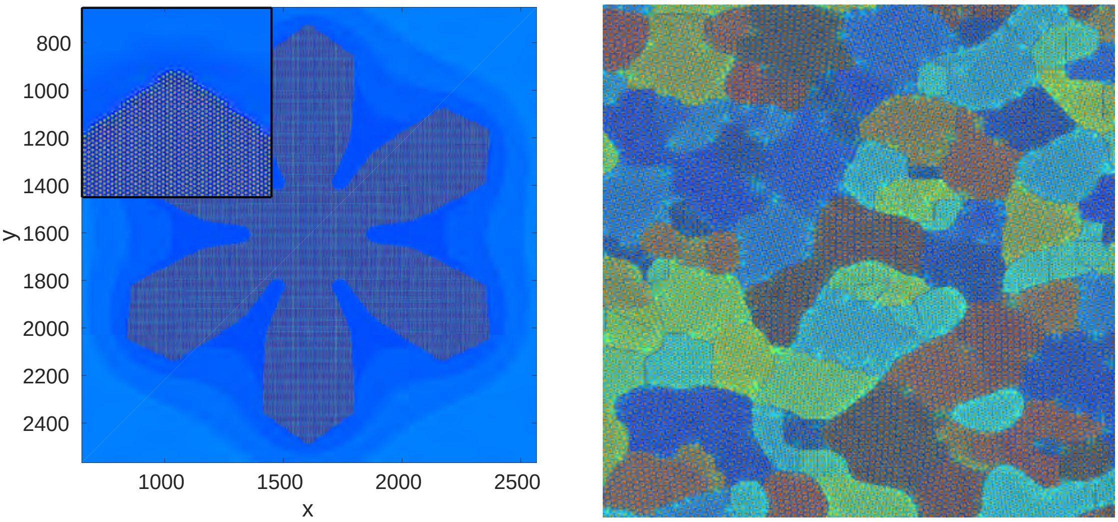

(a) A single crystal grown from a small seed in a supersaturated solution. The hexagonal lattice structure generates an anisotropic surface tension resulting in a large scale structure. The inset is a zoom in showing the crystal lattice.

(b) A polycrystal grown from randomly placed seeds in a supersaturated solution. The individual seeds have been colored according to their orientation.

Figure 2.1: Examples of dynamically grown crystals using (2.7).

while the gradient interaction term can be derived as a continuum limit of a next-nearest neighbour interaction [30]. For quite general $f(\phi)$ it can be shown that the interface in the model is described by the moving boundary equations [31]

$$\frac{\partial \mu}{\partial t} = \Gamma \nabla^2 \mu \tag{2.3}$$

$$\mu = d_0 \kappa + \beta V_n \qquad \text{on } \Lambda \tag{2.4}$$

$$V_n = \left[\frac{\mu}{\partial n}\right]_-^+ \qquad \text{on } \Lambda, \tag{2.5}$$

where the chemical potential is given by $\mu = \delta\mathcal{F}/\delta\phi$, d_0 is the capillary length dependent on the surface tension, κ is the curvature of the interface, β is a kinetic coefficient, V_n is the normal velocity, Λ is the interface position and $[]_-^+$ is the difference between the two sides of the interface. Due to the equilibrium distribution of the concentration field in the bulk regions, it is not straight forward to introduce elastic interactions and lattice properties into the model. To induce an anisotropic surface tension it is necessary to modify the phenomenological constants d_0 and β to depend on the normal orientation of the interface [32], however, introducing elastic interaction as well as motion of defects requires more complex additions to the model [33, 34]

Instead of the above additions to phase field models it is more natural to formulate a theory in which elastic and plastic features such as dislocation motion and anisotropic surface tension are emergent properties from the lattice structure. A simple way to do this is to make the equilibrium configuration a periodic structure similar to a crystal lattice. Interpreting the gradient term above as a lowest order term in a general gradient expansion and using ideas similar to Brazovskii [21], the next order free-energy after integration by parts can be written as

$$\mathcal{F} = \int dV \left[f(\phi) + \frac{\phi}{2} \left(q_0^2 + \nabla^2 \right)^2 \phi \right], \tag{2.6}$$

which coincides with the Swift-Hohenberg free energy [8], where q_0 is the equilibrium wave number. Due to translational invariance all odd gradient terms have been neglected in the general gradient expansion. By assuming the gradient terms originate from an approximation of the two-point correlation function, $\int dr' \phi(r) C_2(r, r') \phi(r') \approx \phi(r) \left(q_0^2 + \nabla^2\right)^2 \phi(r)$, a more formal derivation can be performed by fitting a typical pair-correlation function at liquid solid coexistence and using classical density functional theory of freezing.

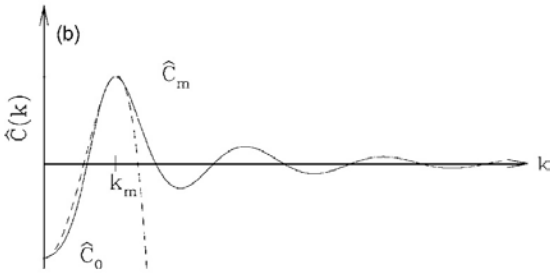

Figure 2.2: A sketch of a typical two-point correlation function at liquid solid coexistence [35]. The dashed line is the approximation discussed in the text, which gives rise to the gradient term in the free energy in (2.6).

This derivation also highlights that the field ϕ should be interpreted as a time averaged atomic density and the bulk free-energy should take the form $f(\phi) = \epsilon\phi^2/2 + \phi^4/4$, which is a truncated expansion of an ideal gas self interaction term [35].

Due to mass conservation the relevant dynamics are of model-B type yielding the equation of motion

$$\frac{\partial \phi}{\partial t} = \nabla^2 \left(\left(q_0^2 + \nabla^2 \right)^2 \phi + \epsilon\phi + \phi^3 \right), \tag{2.7}$$

which together with (2.6) is the simplest form of the Phase Field Crystal model.

As in the case of the Swift-Hohenberg equation, the parameter ϵ can be thought of as a quenching temperature which determines the phase transition between a uniform state to an ordered state. However, due to the conservation of mass in the dynamics it is not only ϵ which determines the phase transition, but also the mean density of the system. The conservation of mass also helps to stabilizes phases other than the striped phase such as a hexagonal and body-centered cubic phase in two and three dimensions and introduces coexistence regions in the phase diagram of the model.

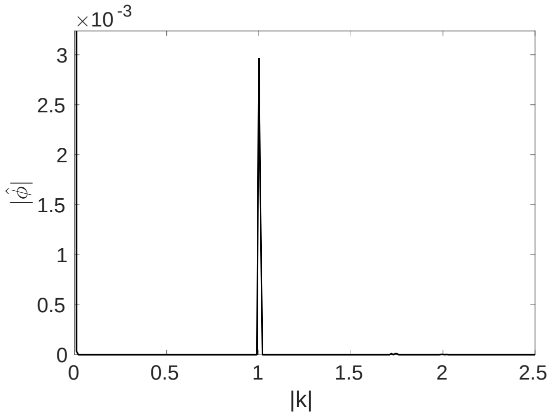

Figure 2.3: The magnitude of the circularly averaged Fourier transform of the density field, $\langle|\hat{\phi}|\rangle$ for an equilibrium structure computed using (2.7). $\langle|\hat{\phi}|\rangle$ has been normalized by the mean density. Notice the dominance of the first peak at $|k| \approx 1$ compared to the next mode at $|k| \approx \sqrt{3}$.

2.1 Static Properties

Some of the static properties of the phase field crystal model such as the phase diagram and the elastic constants, can be analytically studied by substituting a periodic solution into the free-energy in (2.6). In three dimensions the relevant structures in the small ϵ region are planes, hexagonal rods, body-centered cubic and a uniform phase interpreted as a liquid phase. In order to study these structures the density field is expanded as

$$\phi = \phi_0 + \sum_{\mathbf{G}} A_{\mathbf{G}} \exp\left(\mathrm{i}\mathbf{G} \cdot \mathbf{r}\right) + \mathrm{c.c}, \tag{2.8}$$

where ϕ_0 is the mean density, $\mathbf{G}$ is the reciprocal lattice vectors of the different lattices and $A_{\mathbf{G}}$ is the amplitude for each vector. Due to the functional form of (2.6) the equilibrium state is dominated by a single mode corresponding to the smallest $\mathbf{G}$'s in (2.8), as can be seen for a two-dimensional system in fig 2.3. Therefore, when deriving the equilibrium properties only the modes corresponding to the shortest reciprocal lattice vectors will be retained in (2.8).

The phase diagram can be derived by calculating the free-energy for each of the different phases and using Maxwell's common-tangent construction to find the phase transition lines and coexistence regions [29]. In equilibrium the amplitude of the different modes with the shortest reciprocal lattice vector will be equal and a constant. Using the shortest set of reciprocal lattice vectors the uniform, planes, hexagonal and body-centered cubic density expansions are given by

$$\phi_0 = \phi_0 \tag{2.9}$$

$$\phi_1 = \phi_0 + A_1 \cos(qx) \tag{2.10}$$

$$\phi_2 = \phi_0 + A_2 \left(\frac{1}{2} \cos\left(\frac{2qy}{\sqrt{3}} \right) - \cos(qx) \cos\left(\frac{qy}{\sqrt{3}} \right) \right) \tag{2.11}$$

$$\phi_3 = \phi_0 + A_3 \left(\cos(qx) \cos(qy) + \cos(qx) \cos(qz) + \cos(qy) \cos(qz) \right), \tag{2.12}$$

To calculate the equilibrium free-energy, the expansions above are inserted into (2.6) and integrated over one unit cell. The detailed calculation of the functional form of the equilibrium free energy is given in Appendix A. The phase diagram is then found by using Maxwell's common-tangent construction. A sample plot of the liquid and body-centered cubic free energies with a common tangent and the phase diagram is shown in figs 2.4a and 2.4b.

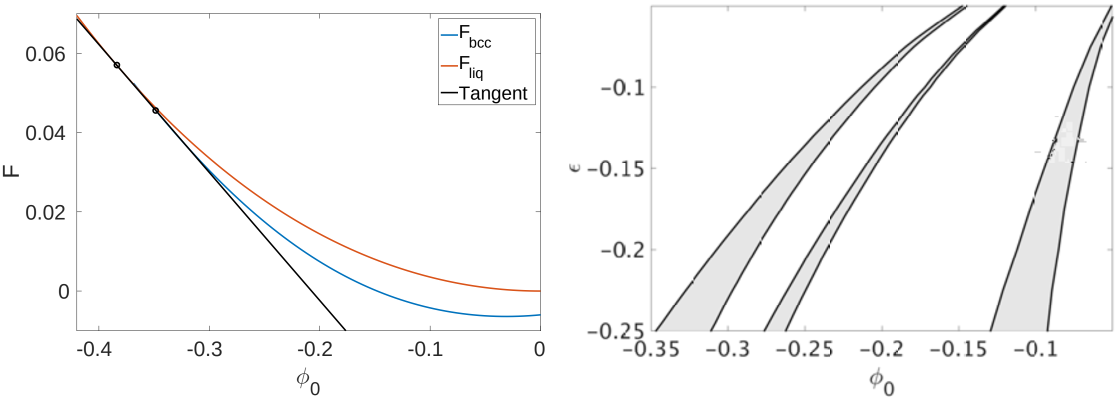

(a) The free-energies of the liquid and body-centered cubic lattice. The intercept with the common tangent determines the coexistence region.

(b) The three-dimensional phase diagram for the phase field crystal model. For smaller ϵ regions of face-centered cubic and hexagonal close packing can also be observed. The white parts from left to right are the regions where the liquid, body-centered cubic lattice, hexagonal rods and planes are the stable configuration, respectively.

Figure 2.4: Static properties of the phase field crystal model in three dimensions.

To derive the elastic coefficient for the equilibrium structures the amplitude expansions is perturbed by a small arbitrary vector and once again inserted into the free-energy [36]. In order to get the elastic constant known from continuum elasticity theory it is necessary to coarse grain the free energy over one unit cell, which amounts to ignoring cross coupling terms such as $A_i A_j$ in the free-energy, since such terms phase factor add up to terms fluctuating on scales smaller than the lattice spacing. For the calculation of the elastic coefficients only the integral over the gradient term $\left(q_0^2 + \nabla^2\right)^2$ needs to be evaluated since it is the sole contributor to the elastic properties. Inserting the amplitude expansion (2.8) into (2.6) with the perturbed amplitude $A_j = A_{eq} \exp\left(i\mathbf{G}_j \cdot \mathbf{u}\right)$, where A_{eq} is the amplitude of the equilibrium state and $\mathbf{u}$ is an arbitrary displacement vector, the gradient terms become

$$\begin{aligned}
&\int dV \sum_j \frac{1}{2}\left(A_j^* \mathcal{L}_j^2 A_j + A_j \left(\mathcal{L}_j^*\right)^2 A_j^*\right) \\
&= \int dV \sum_j \left(\left(\nabla^2 \mathbf{G}_j \cdot \mathbf{u}\right)^2 + 4\left(\frac{1}{2}|\nabla \mathbf{G}_j \cdot \mathbf{u}|^2 + \mathbf{G}_j \cdot \nabla \mathbf{G}_j \cdot \mathbf{u}\right)^2\right) A_{eq}^2 \\
&\approx \int dV \sum_j 4\left(\mathbf{G}_j \cdot \nabla \mathbf{G_j} \cdot \mathbf{u}\right)^2 A_{eq}^2, \qquad (2.13)
\end{aligned}$$

where $\mathcal{L}_j$ is defined by $A_j^* \exp(-i\mathbf{G}_j \cdot \mathbf{r})\left(1+\nabla^2\right)^2 A_j \exp(i\mathbf{G}_j \cdot \mathbf{r}) = A_j^* \mathcal{L}_j^2 A_j$ and explicitly given by $\mathcal{L}_j = \nabla^2 - 2i\mathbf{G}_j \cdot \nabla$. The last approximation in (2.13) is done assuming small displacements on long wave lengths. Using (2.13) and the definition $\sigma_{ij} = \delta\mathcal{F}/\delta u_{ij}$ the stress-strain curves of the model can be derived. In fig 2.5 the stress-strain curve for an area preserving strain in two dimensions is shown.

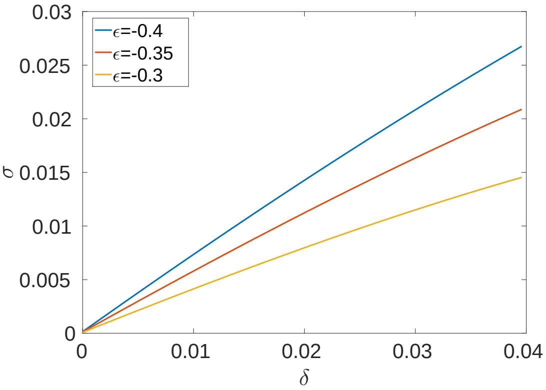

Figure 2.5: The stress-strain curve for a two dimensional hexagonal lattice under an area preserving strain for different quenching temperatures.

In general the elastic free energy can be written as [37]

$$\mathcal{F}_{el} = \frac{1}{2}\int dV C_{ijkl} u_{ij} u_{kl}, \qquad (2.14)$$

where C_{ijkl} is the elastic constant tensor and $u_{ij} = \frac{1}{2}\left(\partial_i u_j + \partial_j u_i\right)$ is the linear strain tensor. Inserting the shortest reciprocal lattice vectors for the body-centered cubic lattice the elastic contribution becomes

$$\begin{aligned}
\int dV \sum_j 4\left(\mathbf{G}_j \cdot \nabla \mathbf{G_j} \cdot \mathbf{u}\right)^2 A_{eq}^2 =& 4\Big(\left(u_{xx}^2 + u_{yy}^2 + u_{zz}^2\right) + 2\left(u_{xy}^2 + u_{yz}^2 + u_{xz}^2\right) \\
&+ \left(u_{xx}u_{yy} + u_{xx}u_{zz} + u_{yy}u_{zz}\right)\Big) A_{eq}^2 \qquad (2.15)
\end{aligned}$$

from which the elastic constants can be read off as, $C_{xxxx} = C_{yyyy} = C_{zzzz} = 8A_{eq}^2$ and $C_{xxyy} = C_{xxxx}/2$ and similarly for the rest of the off-diagonal constants which is the symmetry expected for a body-centered cubic lattice with A_{eq} given in (A.14). Similarly the two-dimensional hexagonal lattice vectors can be substituted into (2.13) yielding their elastic constants, which are also found to obey the relevant symmetry of the lattice. In the uniform liquid phase the equilibrium-amplitude is zero such that the elastic constants self-consistently vanish. It can be shown that the free-energy (2.6) also gives the correct non-linear elastic behaviour, when retaining the full differential operator instead of using the long wavelength approximation in (2.13) [38].

Further static properties of the free-energy (2.6) such as an anisotropic surface tension between the liquid and the crystal state can with some effort also be shown to be an emergent feature of the one-mode dominance of the model and the inherent lattice structure in the equilibrium density distribution [39].

The accuracy of the phase diagram, elastic coefficients and surface tensions all derived with the one mode approximation have been tested and found to be reasonably accurate for small ϵ [7, 13, 40].

Apart from analytic results, a large amount of numerical studies have been performed in order to quantify the static properties of the crystal structures in the phase field crystal model. To name a few, it has been shown that the grain boundary energy obeys the Read-Shockley relation for the energy associated with two neighbouring grains with a small mutual misorientation [13] and the reverse Hall-Petch effect known from nano scale materials, where the yield stress increases with increasing gain size, was found and studied in [41].

2.2 Coarsening Dynamics

Most macroscopic materials consist of an assembly of small crystal grains of different lattice orientation and sizes. The properties of these polycrystalline materials are highly dependent on grain sizes and grain boundaries. Grain boundaries in polycrystals have been studied for a long time both experimentally [42] and numerically [43]. These materials typically form from the nucleation and growth of grains with different lattice orientations in a quenched or annealed melt. Depending on temperature and external forces such as an applied stress, these grain boundaries can become mobile and will rearrange in time. When the grain boundaries are mobile the polycrystalline matrix starts to coarsen in time, reducing grain boundary length by eliminating smaller grains while larger grains becomes bigger.

There have been multiple attempts at theoretically modelling the grain coarsening mechanism in polycrystals. Classically grain growth in two dimensions have been assumed to be driven by the minimization of the surface energy resulting in a power-law coarsening given by $\langle L\rangle \sim t^{1/2}$ [44], where L is a characteristic length scale for the domains in the system. However, in three dimensions the increased geometrical complexity does not allow for a simple universal growth law [45, 46]. For models described with model-B dynamics general arguments set the upper bound for coarsening dynamics in higher dimensions as $\langle L^D \rangle \sim t^{D/2}$, coinciding with the surface energy minimization models in two dimensions [27], implying that the classical coarsening exponent of 1/2 is an extremal exponent for coarsening dynamics.

General domain coarsening has been widely studied numerically using model-A and model-B type of models with equations of motion given by

$$\frac{\partial \phi}{\partial t} = -\left(\nabla^{2n}\right)^n \frac{\delta \mathcal{F}}{\delta \phi}, \tag{2.16}$$

where $n = 0$ is model-A type and $n = 1$ is model-B type. For the simple case of uniform bulk regions described by the free energy $\mathcal{F} = \int dV \left(f(\phi) + \frac{K}{2} |\nabla \phi|^2 \right)$, the coarsening follows a power law $\langle r \rangle \sim t^\alpha$ with exponent $\alpha = 1/2$ and $\alpha = 1/3$ for model-A and model-B, respectively. The evolutions of roll patterns have been investigated in several numerical studies using model-A dynamics finding the coarsening exponent to be $\alpha = 1/4 - 1/5$ [47–49].

Two dimensional coarsening in the phase field crystal model has also been studied in [50, 51], finding coarsening exponents in the range $\alpha = 1/4 - 1/20$. Furthermore, it was found that the coarsening exponents to some degree were time-dependent. The large spread in coarsening exponents suggests that the coarsening mechanism is quite different from model-A to model-B types of models. In [50] we found that supplementing the slow coarsening rate was also a stagnating regime, where the coarsening dynamics for general initial conditions stopped all together, see fig 2.6a. This behaviour is in contrast to the theoretical modelling of coarsening dynamics, which predicts perpetual domain growth. Based on molecular dynamics simulations it has been argued that the roughness of the grain-boundary controls the grain growth, and that the presence of a small fraction of low-mobility, smooth grain boundaries can lead to stagnation [52].

In order to quantify the grain dynamics in the coarsening and stagnation regime we measured the change in orientation and grain area for each grain. In fig 2.6b the mean orientational change is plotted from which it is seen that rotation plays an important part in the coarsening dynamics in this model. To further quantify rotation for the individual grains, it was found that in general change in the ratio of the change in orientation over change in area followed a power law as

$$\left| \frac{\Delta \theta}{\Delta A} \right| \sim A^{-\beta_2}, \tag{2.17}$$

with the exponent $\beta_2 = 1.25 \pm 0.06$. In comparison, the expected exponent for grain rotation obeying conservation of dislocations is given by $\beta = 3/2$ [53], implying that to a high degree the coarsening dynamics obeys conservation of dislocations.

The high dependence on grain rotation and the large spread in the coarsening exponent suggests that the power law coarsening is non-universal with respect to the temperature parameter ϵ in two dimensions. Instead, the dynamics of the combination of local grain rotation and grain growth was shown to be independent of ϵ. Experimentally, both rotation as well as a large spread in coarsening exponents have also been found [54, 55].

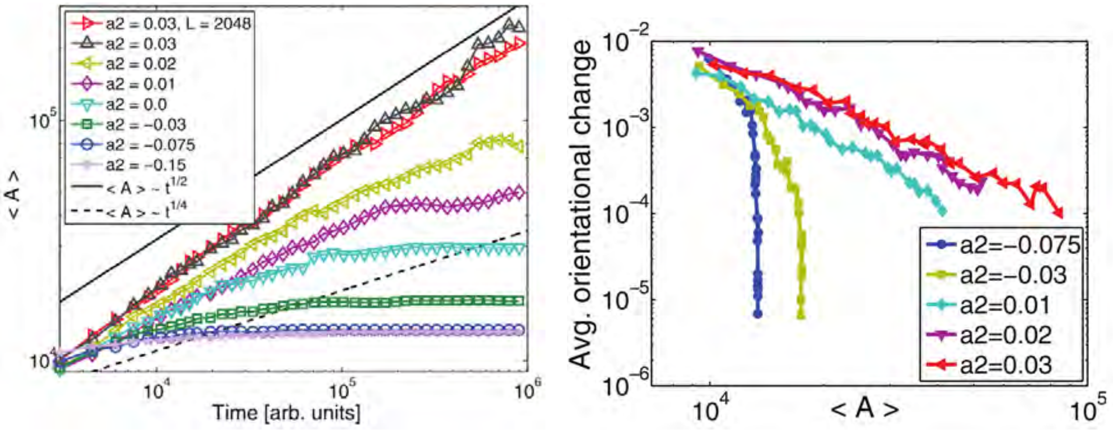

(a) The mean grain size as a function of time for systems at different quenching temperatures. In this formulation of PFC $a_2 \sim \epsilon$. There is a continuous decrease in coarsening exponent towards the stagnating state.

(b) The average rotational change as a function average mean grain area. For systems close to the melting temperature the grain coarsening is supplemented by a decrease in grain rotation. Stagnating systems is characterized by a rapid decrease in mean grain rotation.

Figure 2.6: Results from coarsening study in two dimensions [50]

In [56] we generalized the study of coarsening dynamics to three dimensional coarsening of crystals with body-centered cubic symmetry. We once again observed a cross-over from a stagnating regime to a coarsening regime both greatly influenced by grain rotation. The initial dynamics for the stagnating regime was once again found to be supplemented by a decrease in the amount of average rotation in the system until complete stagnation was reached as shown in fig 2.8c.

In the coarsening regime the grain size distribution was found to be highly heterogeneous with a few large grains growing faster than the rest of the crystal matrix resulting in abnormal grain growth, see figs 2.8a and 2.8d. Similar dynamics have been reported in both numerical as well as experimental studies [57, 58].

Independent of the quenching temperature parameter, it was found that the ratio of the change in orientation over the change in volume followed a power law as

$$\left|\frac{\Delta\theta}{\Delta V}\right| \sim V^{-\beta_3}, \tag{2.18}$$

with exponent $\beta_3 = 1.24 \pm 0.06$. In three dimensions the geometrical arguments from [53] for shrinking rotating crystals obeying conservation of dislocations implies an exponent of

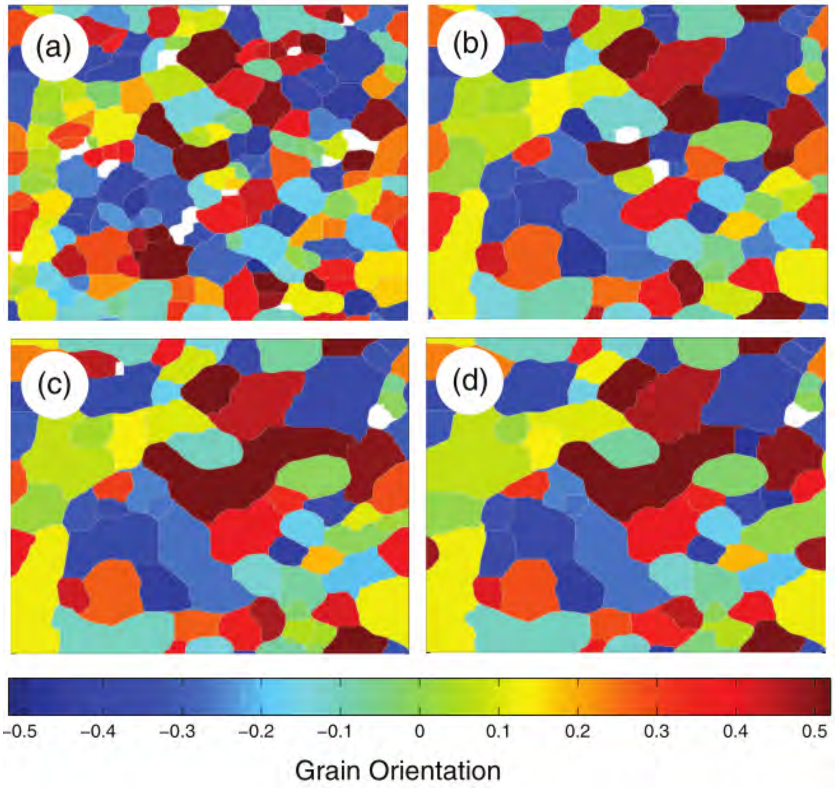

Figure 2.7: Snapshot of the evolution of a polycrystal. The colour denotes the individual grains lattice orientation[50].

$\beta_3 = 4/3$ in fair agreement with the measured quantity.

The coarsening regime was found to be further divided between an initial power law coarsening with a transition to exponential coarsening, see fig 2.8b. To explain this behaviour, consider a model where the coarsening is predominantly due to grain coalescence of rotating grains. Introducing a characteristic time for coalescence, t_l, the dynamics of the number of grains can be described by

$$\frac{1}{N}\frac{dN}{dt} = -\frac{1}{t_l}, \tag{2.19}$$

where N is the number of grains. Assuming that t_l is inversely proportional to the mean grain rotational velocity $1/\langle\Delta\theta\rangle$ and that we have the relation $\langle\Delta\theta\rangle = Ct^{\gamma}$ while using the conservation of volume $N(t)\langle V\rangle = V_{sys}$, the average volume can be shown to be given by

$$\langle V(t)\rangle = V_0\left(\frac{t}{t_0}\right)^{CK_\theta}, \qquad \gamma = -1 \tag{2.20}$$

$$\langle V(t)\rangle = V_0 \exp\left(\frac{CK_\theta}{(\gamma+1)}\left(t^{\gamma+1} - t_0^{\gamma+1}\right)\right), \qquad \gamma \neq -1 \tag{2.21}$$

where K_θ is a dimensionless constant describing the time scale over which grain rotation will result in coalescence between neighbouring grains. As shown in fig 2.8c the coarsening regime shows little to no decrease in average rotation during the time evolution and consequently it is to be expected from (2.21) that the system exhibits exponential coarsening. Extracting C and CK_θ from figs 2.8b and 2.8c we find that C scales linearly with ϵ and for $K_\theta \sim 40$ the two curves collapse consistent with the assumption that grain growth is predominantly mediated by grain rotation and coalescence.

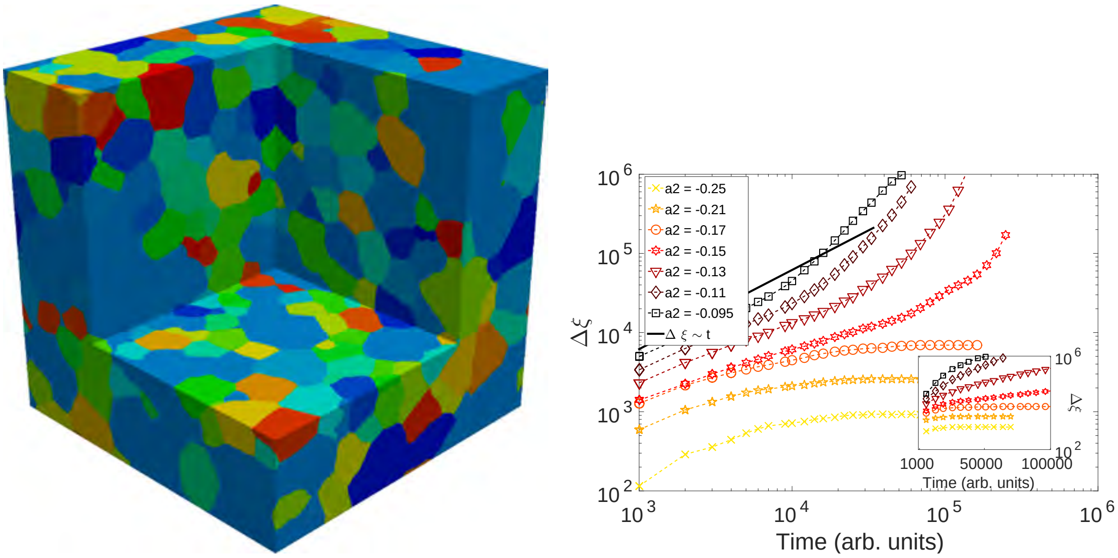

(a) A snapshot of a three-dimensional polycrystal. The convoluted grain geometry of some of the grains is a sign of coalesced grains due to rotation. The color is only a label for the different grains.

(b) The time evolutions of the coarsening parameter on double logarithmic axes. The inset is the same data on semilogarithmic axes, showing the transition to exponential coarsening. Note $a_2 = \epsilon$.

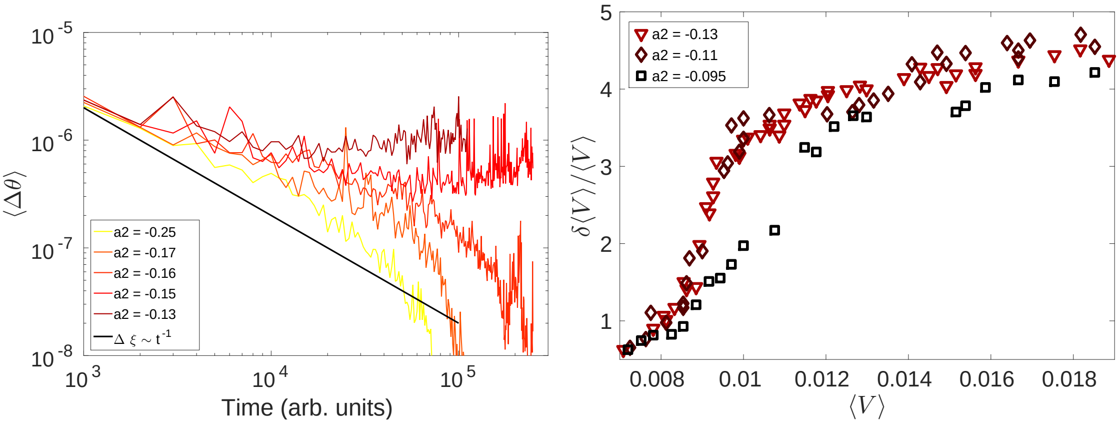

(c) The average rotational velocity for individual grains. The straight line corresponds to a power law with exponent $\alpha = -1$.

(d) Ratio of the standard deviation in grain size and the mean size as a function of mean size. For self-similar growth the standard deviation on the grain volumes increases proportionally to the mean grain volume. The non-constant evolution is a sign of abnormal grain growth.

Figure 2.8: Results from coarsening study in three dimensions [56].

Recently, it has been argued that the dynamical equation in (2.7) is not appropriate for real crystal dynamics [59]. Due to the lack of Galilean invariance in (2.7), rotation of an equilibrium density distribution produces an energy dissipation contrary to atoms governed by Newton's Second Law for which there is no energy dissipation associated with rotation of a grain. It can be shown that the anomalous energy dissipation scales with the area in two dimensions and the volume in three dimensions of a grain and is supposed to suppress rotation of large-scale structures. For single grain inclusion experiments the energy dissipation results in a grain shrinkage rate dependent on the size of the grain, which was interpreted as a possible reason for the small coarsening exponents measured in coarsening experiments using the free energy in (2.6). However, in [56] we found a large degree of rotation on all grain size scales as well as exponential coarsening due to the rotation and coalescence of grains. Therefore, it is not entirely clear at what scales the anomalous dissipation becomes an important factor for three dimensional coarsening in polycrystals.

2.3 Plasticity and Dislocation Dynamics

Polycrystalline materials exhibit complex plastic deformation behaviour due to the non-trivial response of single crystals to external forces. Contrary to the smooth macroscopic plastic flow, small-scale deformations of single crystals is highly intermittent in time and heterogeneous in space. Experimentally it has been found that the small-scale deformations are characterized by strain-rate fluctuations and strain avalanches, which obey scale free power law statistics [60, 61].

The macroscopic deformations can be linked to the microscopic dislocation dynamics using for example acoustic emission measurements of crystals under external loads which links the amplitude of the emission to the collective motion of dislocations using the connection [60, 61]

$$A \sim b\rho_d \langle \mathbf{v} \rangle = \dot{\gamma}, \tag{2.22}$$

where A is the measured amplitude, b is the magnitude of the Burgers vector for the dislocations, ρ_d is the density of mobile dislocations, $\langle \mathbf{v} \rangle$ is the mean velocity of dislocations and $\dot{\gamma}$ is the strain rate which is related to the other quantities through Orowan's relations.

Due to the lattice properties of the density field in the phase field crystal model, dislocation creation and annihilation are emergent characters of the model contrary to more traditional approaches such as discrete dislocation dynamics models [**?**], which makes it an alternative choice for investigating dislocation dynamics. However, in order to investigate the dynamics of dislocations, the equation of motion has to be generalized. The simple form of equation (2.7) propagates all disturbances in the density field diffusively. This includes elastic and plastic deformation as well as disturbances in the density field due to grain boundary motion. In real

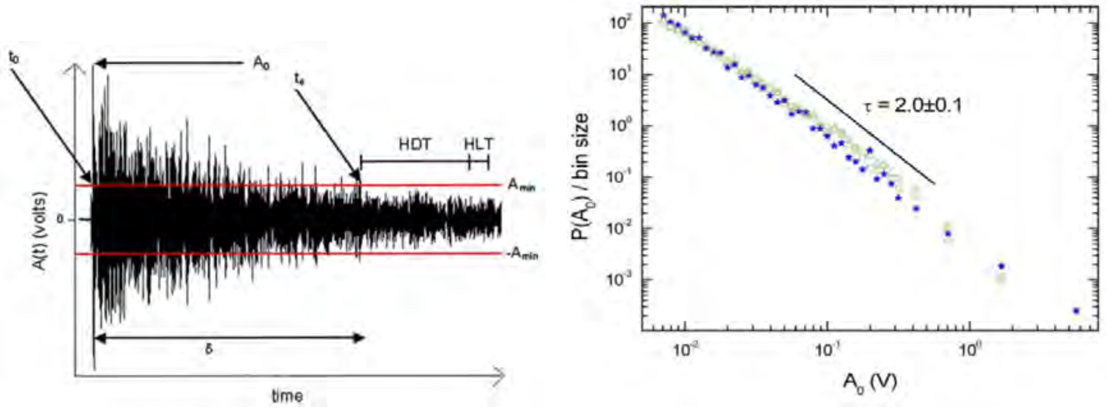

(a) Acoustic emmision signal.

(b) Probabillity distribution of the maximum amplitude in an avalanche.

Figure 2.9: Results from an ice compression experiment[61].

materials the relaxation of elastic strains happens on a time scale much faster than the diffusive propagation. In order to include a faster propagation mechanism equation (2.7) was modified to [62]

$$\frac{\partial^2 \phi}{\partial t^2} + \beta \frac{\partial \phi}{\partial t} = \alpha^2 \nabla^2 \left(\left(q_0^2 + \nabla^2 \right)^2 \phi + \epsilon \phi + \phi^4 \right) . \tag{2.23}$$

Choosing the effective speed of sound α and the damping coefficient β, it is possible to set an elastic interaction and time scale over which waves in the density field will propagate undamped after which the density disturbance will become diffusive again. In this way it is possible to have dynamics including rapid elastic relaxation and large scale diffusion evolution.

Equation (2.23) has been used to study the event energy distribution of avalanches of a sheared crystal [63]. Using a shearing term employed at the boundary of the simulation box, it is possible to shear a perfect crystal until the crystal breaks and dislocations are created. Measuring the total velocity of dislocations $V(t) = \sum_i^N |\mathbf{v}_i|$ the event energy was extracted by thresholding $V(t)$ and calculating $\int_{t_i}^{t_f} V(t)^2 dt$. It was found that the energy distribution followed a power law as $P(E) \sim E^{\tau}$ with $\tau = 1.5$ in agreement with experimental results [64, 65], implying that the distribution of energy in dislocation mediated avalanches is correctly described in the phase field crystal model.

In [66] we used the emergent dislocation dynamics to study the fluctuations in the number density of dislocations using the modified dynamical equation (2.23) in a sheared crystal. We used the same boundary conditions as in [63] to shear a perfect crystal in order to generate dislocations. In a perfect two dimensional hexagonal lattice every atom will have six nearest neighbours. An easy method to locate dislocations is to use a Voronoi tessellation to find atoms with five and seven nearest neighbours, see fig 2.10. Due to annihilation and creation events the density of dislocations becomes a fluctuating variable, whose power spectrum was found to follow a power law with exponent -2 as shown in fig 2.11a. The probability distribution of the number of dislocations was shown to be unimodal for large shearing rates while for lower rates the distribution becomes bimodal as shown in fig 2.11b. In order to explain the probability distribution we introduced a Langevin equation for the density of dislocations given by

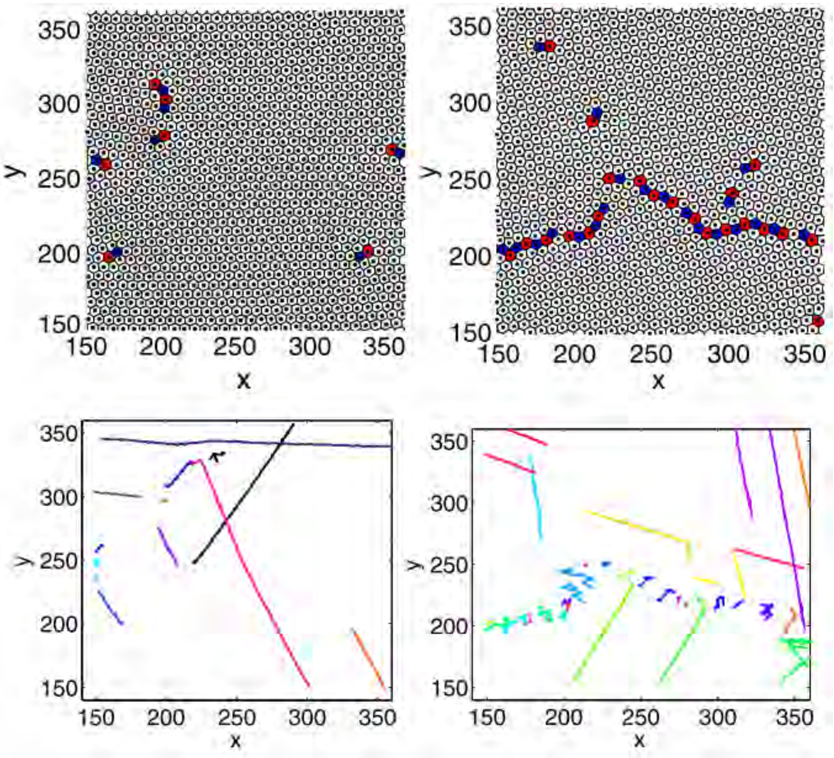

Figure 2.10: Different dislocation configurations visualized using a Voronoi tessellation together with the trajectories of the dislocations. The left panel is in the regime of slow shear rate with a dilute configuration with fast moving dislocations. The right panel shows a more dense distributions with dislocations assembled into grain boundaries [66].

$$\frac{d\rho_d}{dt} = f(\rho_d) + g(\rho_d)\xi(t), \tag{2.24}$$

where ρ_d is the density of dislocations and the noise term is related to dislocation interaction and is approximated by Gaussian white noise with a zero mean and variance given by

$$\langle \xi(t)\xi(t') \rangle = 2D\delta(t - t'), \tag{2.25}$$

where D describes the amplitude of the noise due to interactions. The deterministic part of (2.24) describing the dislocation reaction rate is given by a double-well potential as $f(\rho_d) = -dU(\rho_d)/d\rho_d$ with

$$U(\rho_d) = \frac{1}{4}\left(\frac{\rho_2}{m} - 1\right)^4 - \frac{1}{2}\left(\frac{\rho_d}{m} - 1\right)^2 - \kappa\left(\frac{\rho_d}{m} - 1\right). \tag{2.26}$$

The two minima of the potential corresponds to the state with zero dislocations and a state with a non-zero mean number of dislocations. The scaling parameter m locates the mean number of dislocations and depends on the shear rate. κ is a parameter favouring the state with a finite mean density of dislocations. Finally, the noise intensity in the system should depend on the density of dislocations and is assumed to be a linear approximation $g(\rho_d) = 1 + \rho_d/m$. The steady state solution of the Fokker-Planck equation associated with (2.24) is given by

$$P(\rho_d) = \mathcal{N}\left(1 + \frac{\rho_d}{m}\right)^{-1-11/D} \exp\left(-\frac{\mathcal{L}(\rho_d)}{2D}\right), \tag{2.27}$$

where $\mathcal{N}$ is a normalization constant and $\mathcal{L}(\rho_d) = \frac{\rho_d}{m^2(m+\rho_d)}\left(\rho_d^2 - 9m\rho_d - 2m^2\kappa - 22m^2\right)$. As shown in fig 2.11b this probability distribution gives an excellent fit to the data both in the unimodal as well as bimodel regime. Using the results of [67–69] it can be further shown that the high frequency limit of the power spectrum of the signal generated with (2.24) gives the observed exponent of -2.

Together with [63] our results show that the phase field crystal model is able to generate power law statistics as seen in experimental studies of small-scale plasticity. Furthermore, our results in [66] together with Orowan's relation (2.22) suggests that it is not only the mean velocity of dislocations that plays a role in strain rate fluctuations.

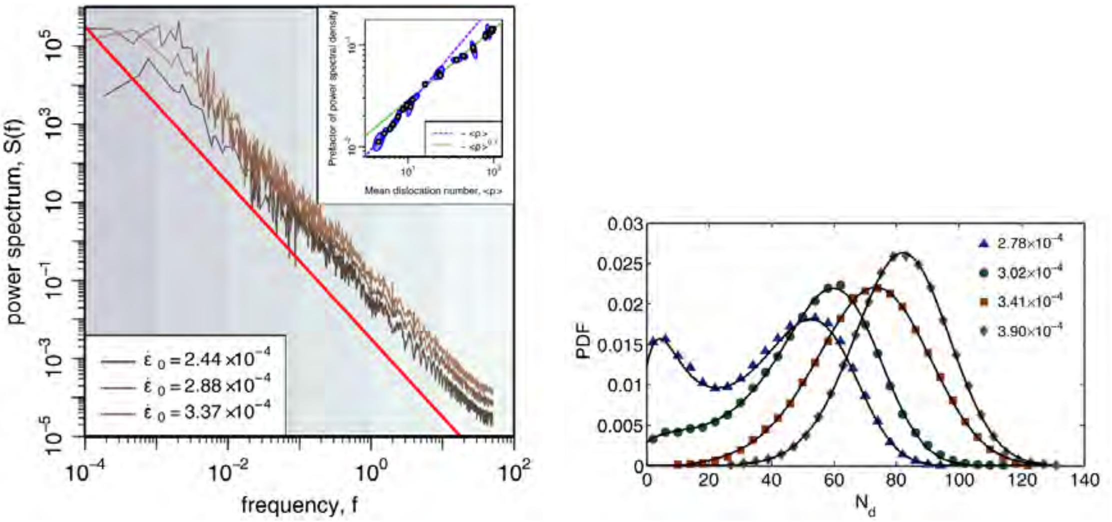

(a) Power spectrum of the dislocations number fluctuations for different strain rates. The red lines shows a power law with exponent -2. The insets shows the constant C as a function of mean dislocation number, with C found be fitting the power spectra to Cf^{-2}. For small mean dislocations number the signal behaves as a sum of uncorrelated dislocations with $C \sim \langle\rho_d\rangle$, with a cross over to a power law scaling for C for higher mean density of dislocations.

(b) Probability distribution of numbers of dislocations for the different shear rates. For low shear rates the systems shows a bimodal behaviour while the distribution becomes unimodal with a well defined mean for higher strain rates.

Figure 2.11: Results for the dislocations dynamics in a two-dimensional sheared crystal [66].

CHAPTER 3

Biological Active Matter

Living material such as schools of fish and flocking birds or on a smaller scale confluent cell layers are a form of active matter being composed of self propelled entities. The complex dynamics exhibited by active matter is in many ways different from classical passive materials such as water and air. Due to the constant energy injection at the local scale of the "particles", these systems are maintained in a perpetual non-equilibrium state that in some instances can lead to large-scale self-organised patterns and turbulent-like dynamics. This behaviour is contrary to classical non-equilibrium systems, which in most situations is driven by imposed boundary conditions such as an applied stress or other external forces.

An early model for studying self-propelled active systems is the particle-based Vicsek model [70] which has been used to describe the movements of locusts [71] as well as the landing of flocking birds [72]. In its simplest form the model describes particles that are self-propelled maintaining a constant speed with its orientation being dependent on the orientation of its immediate neighbours. The local aligning interaction will eventually lead to swarming behaviour, demonstrating that large-scale behaviour can emerge from very simple local interaction rules, as shown in fig 3.1

Models based on hydrodynamics serve as an alternative to particle based approaches. For cells suspended in a liquid medium these models are a natural starting point.

Using the simplifying assumption that a cell moves in a completely overdamped medium, highly specific models for cell dynamics and the resulting velocity field of the fluid can be developed. In this case, the general Navier-Stokes equation reduces to the linear Stokes equation and the cell movement can be approximated by a sum of fundamental solutions to the Stokes equation [73]. For a general system of dilute cell suspension the cell density can be coupled to the full Navier-Stokes equation from which a Fokker-Planck equation for the probability density function of the swimming direction of the cells can be derived [74].

A completely phenomenological approach to modelling active matter phenomena, and es-

Figure 3.1: For some parameters the Vicsek model displays flocking behaviour [70]. The velocities of the particles are shown by an arrow.

pecially flocking, was given in [3] where the equation of motion of a velocity field for the collective motion of the flock was expanded in a gradient expansion to second order under the assumption that the equations of motion should be rotationally invariant. By sacrificing Galilean invariance it is possible to include a generalized material derivative as well as a potential term driving the system towards a mean velocity. The full set of equations can be seen as a generalized Navier-Stokes type of equation given by

$$\begin{aligned}\frac{\partial \mathbf{v}}{\partial t} &+ \lambda_1 (\mathbf{v}\cdot\nabla)\mathbf{v} + \lambda_2 (\nabla\cdot\mathbf{v})\mathbf{v} + \lambda_3 \nabla|\mathbf{v}|^2 = -\nabla p - \left(\alpha + \beta|\mathbf{v}|^2\right)\mathbf{v} \\ &+ D_B \nabla(\nabla\cdot\mathbf{v}) + D_T \nabla^2 \mathbf{v} + D_2 (\mathbf{v}\cdot\nabla)^2 \mathbf{v} + \mathbf{f} \qquad (3.1) \\ \frac{\partial \rho}{\partial t} &+ \nabla\cdot(\mathbf{v}\rho) = 0, \qquad (3.2)\end{aligned}$$

where $\mathbf{v}$ is the velocity, ρ is a density, and $\mathbf{f}$ is a random driving force. In principle all the constants can depend on ρ and $|\mathbf{v}|^2$. The left hand side of (3.1) is the generalized material derivative. On the right hand side p is the pressure, which for incompressible fluids is determined by $\nabla\cdot\mathbf{v} = 0$. For compressible fluids another equation relating p to ρ or $\mathbf{v}$ is needed. The gradient terms are a general second-order expansion accounting for viscous effect in the system due to particle interactions. Finally, the local term parametrized by α, β can be interpreted as originating from a Landau type potential

$$U(|\mathbf{v}|) = \frac{\alpha}{2}|\mathbf{v}|^2 + \frac{\beta}{4}|\mathbf{v}|^4, \qquad (3.3)$$

where stability requirements demand $\beta > 0$. For $\alpha > 0$, the potential is a single well potential describing a system with mean velocity at the minima in $|\mathbf{v}| = 0$, while for $\alpha < 0$ the potential is a double-well giving rise to a non-zero mean velocity at the minima in $|\mathbf{v}| = \sqrt{-\alpha/\beta}$. Equation (3.2) is a continuity equation making the set of equations satisfy mass conservation. While there is no physical microscopic origin of the different terms or parameters in equation (3.1), its generality has made it possible to use it as a starting point for modelling a wide range of active matter phenomena [75].

Recently, a generalization of (3.1) has been used in the study of the dynamics of bacteria in a dense suspension and the dynamics of an endothelial cell layer [4, 5]. Experiments with active matter have found the emergence of a characteristic vortex distance and turbulent like dynamical behaviour with long spatial correlations [76].

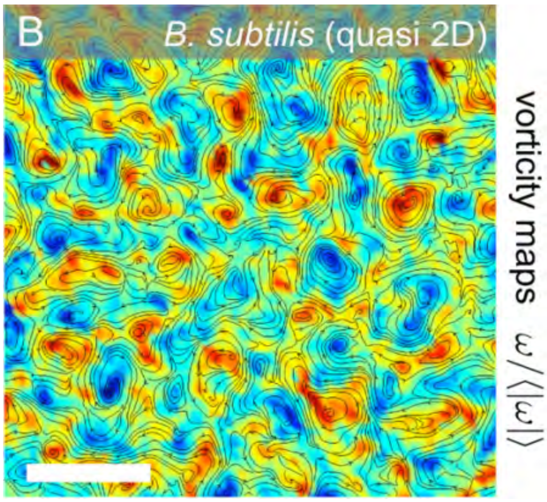

Figure 3.2: The vorticity field for a highly concentrated two-dimensional bacterial suspension[4]. Scale bar is 50μm.

In classical fluid dynamics turbulent flow and vortex structures arise from imposed boundary conditions in the limit of large Reynolds numbers, corresponding to large inertial forces compared to the viscous forces [77]. In contrast, the estimated Reynolds number for an endothelial cell layer showing turbulent-like behaviour can be estimated to $Re = 10^{-9}$ [5], and is an emergent feature independent of imposed boundary conditions. It has been found that one way to enable that equations similar to (3.1) can describe low Reynolds number turbulence is to extend the gradient expansion from second order to fourth order.

3.1 Cell Division in an Endothelial Cell Layer.

Endothelial cells line the blood vessels in a tightly bound layer causing the cells to have a highly collective dynamic behaviour. Due to the tight adhesion, mechanical forces are transmitted over large distances [78], which can serve as a guide for the cells as they most often prefer to migrate in the direction of least shear stress [79] and seem to navigate towards empty spaces [80]. In ref. [5] we investigated the influence of cell division of endothelial cells on the collective dynamics of the cell layer. The cell layer was modelled using a hydrodynamics approach, while cell division was described by a localized energy injection.

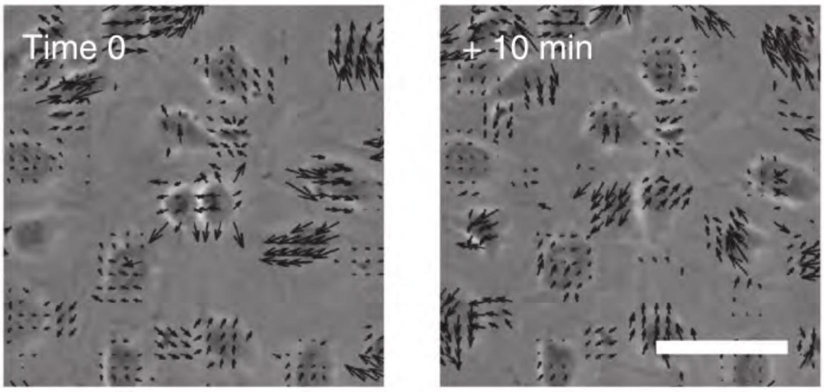

Figure 3.3: Velocity field around a cell division in an endothelial cell layer. The left picture is right after the division of the cell in the center while the picture to the right is ten minutes later. The white scale bar is 50μm

For an endothelial cell layer the higher order extension of (3.1) starts out by assuming the active matter obeys the general momentum balance equations for constant density given by

$$\frac{\partial \mathbf{v}}{\partial t} = \frac{1}{\rho}\nabla \cdot \sigma - \left(\alpha + \beta|\mathbf{v}|^2\right)\mathbf{v}, \tag{3.4}$$

where ρ is the density, $\mathbf{v}$ is the local velocity and σ is the stress tensor. The second term on the right hand side is once again a potential term driving the system towards a mean velocity. For an endothelial cell layer the cells move with an average velocity, implying that $\alpha < 0$ and $\beta > 0$ with the characteristic cell velocity given by $v_c = \sqrt{-\alpha/\beta}$. Assuming the projected area of each cell is conserved, the velocity field in (3.4) will be incompressible and obeys $\nabla \cdot \mathbf{v} = 0$. In order to describe the dynamical pattern formation, the stress tensor is generalized beyond the Newtonian fluid approximation. The higher order stress tensor is taken to be [4]

$$\sigma_{ij} = -p\delta_{ij} + \eta_0\left(\frac{\partial v_j}{\partial x_i} + \frac{\partial v_i}{\partial x_j}\right) - \eta_2\nabla^2\left(\frac{\partial v_j}{\partial x_i} + \frac{\partial v_i}{\partial x_j}\right) + S\left(v_i v_j - \frac{\delta_{ij}}{D}|\mathbf{v}|^2\right), \tag{3.5}$$

where p is the pressure and the subscripts denote coordinates. The second and third terms are the viscosity terms. The last term is a nematic term similar to the Q-tensor for nematic crystals [81], with S being a fitting parameter, which in our case was found to be $S/\rho = 2.1 \pm 0.2$ and D is the dimension of the system. In the endothelial cell layer the cells continuously inject energy at the cell length scale when moving due to the effect of viscosity. In accordance with the analysis of classical higher-order differential equations [8, 15, 21], we model this by letting

$\eta_0 < 0$ while keeping $\eta_2 > 0$, thereby generating a non-zero maxima in the linear dispersion relation of (3.4). In our experiment the relevant length scale introduced into the dispersion relation is the cell scale. Inserting (3.5) into (3.4) we get the equations of motion

$$\frac{\partial \mathbf{v}}{\partial t} = -\frac{1}{\rho}\nabla p + \frac{S}{\rho}\left(\mathbf{v}\cdot\nabla\right)\mathbf{v} - \frac{S}{\rho D}\nabla|\mathbf{v}|^2 + \nu_0\nabla^2\mathbf{v} - \nu_2\nabla^4 - \left(\alpha + \beta|\mathbf{v}|^2\right)\mathbf{v} \tag{3.6}$$

$$\nabla\cdot\mathbf{v} = 0, \tag{3.7}$$

where $\nu_0 = \eta_0/\rho$ and $\nu_2 = \eta_2/\rho$.

Taking the curl of (3.6) and linearising around $\mathbf{v} = 0$, the equation of motion for the vorticity in two dimensions becomes

$$\frac{\partial \omega}{\partial t} = -\nu_2\left(\nabla^2 - \frac{\nu_0}{2\nu_2}\right)^2\omega - \left(\alpha - \frac{\nu_0^2}{4\nu_2}\right), \tag{3.8}$$

where $\omega = \nabla\times\mathbf{v}$ is the vorticity. For $\nu_0 < 0$, equation (3.8) coincides with the linear part of a Swift-Hohenberg type of equation [8], generating vorticity structures with a wavelength of $2\pi\sqrt{-2\nu_2/\nu_0}$. For our experimental set-up this wavelength was set to approximately 1.5 cell diameters corresponding to the tendency of nearby cells to rotate in opposite directions.

For $\alpha < 0$ equation (3.6) has two uniform steady states. The isotropic state with $\mathbf{v} = 0$ and the polar state with $\mathbf{v} = \mathbf{v}_0$ where $|\mathbf{v}_0| = \sqrt{-\alpha/\beta}$. To examine the stability of the uniform fixed points, equation (3.6) and (3.7) are expanded around the two steady-state solutions.

Perturbing around the zero solution as $\mathbf{v} = 0 + \delta\mathbf{v}$ and $p = p_0 + \delta p$, where p_0 is a constant, equation (3.6) and (3.7) reduces to first order in the perturbations to

$$\nabla\cdot\delta\mathbf{v} = 0 \tag{3.9}$$

$$\frac{\partial \delta\mathbf{v}}{\partial t} = -\nabla\delta p - \alpha\delta\mathbf{v} + \nu_0\nabla^2\delta\mathbf{v} - \nu_2\nabla^4\delta\mathbf{v}. \tag{3.10}$$

Considering perturbations of the form $(\delta\mathbf{v}, \delta p) = (\delta\hat{\mathbf{v}}, \delta\hat{p})\exp\left(i\mathbf{k}\cdot\mathbf{r} + \sigma t\right)$, the above equations reduce to

$$\mathbf{k}\cdot\delta\hat{\mathbf{v}} = 0 \tag{3.11}$$

$$\sigma\delta\hat{\mathbf{v}} = -i\mathbf{k}\delta\hat{p} - \left(\alpha + \nu_0 k^2 + \nu_2 k^4\right)\delta\hat{\mathbf{v}}, \tag{3.12}$$

where $k = |\mathbf{k}|$. Using the incompressibility condition (3.11) leads to $\delta\hat{p} = 0$ and

$$\sigma(k) = -\left(\alpha + \nu_0 k^2 + \nu_2 k^4\right). \tag{3.13}$$

For $\sigma(k) > 0$ perturbations will exponentially grow implying that the fixed point $(\mathbf{v}, p) = (0, p_0)$ is unstable. The range of stable wave numbers is found by solving $\sigma(k) = 0$ whose solutions are

$$k_\pm^2 = \frac{|\nu_0|}{\nu_2}\left(\frac{1}{2} \pm \sqrt{\frac{1}{4} - \frac{\alpha\nu_2}{\nu_0^2}}\right), \qquad \text{for} \quad \alpha < \frac{\nu_0^2}{4\nu_2}. \tag{3.14}$$

For $\eta_0 < 0$ and $\eta_2 > 0$ the fixed point will have a band of unstable wavenumbers as shown in fig 3.4a.

For the other fixed point equation (3.6) and (3.7) are expanded around $\mathbf{v} = \mathbf{v}_0 + \delta\mathbf{v}$ and $p = p_0 + \delta p$. To simplify the analysis the constant vector is rotated to align with the x-axis $\mathbf{v}_0 = (v_0, 0)$ and the perturbation to $\delta\mathbf{v} = (\epsilon_{\parallel}, \epsilon_{\perp})$. Inserting the perturbations into (3.6) and using the relation $v_0 = \sqrt{-\alpha/\beta}$ the linear order equation becomes

$$\mathbf{k} \cdot \delta\hat{\mathbf{v}} = 0 \tag{3.15}$$

$$\frac{\partial \delta\mathbf{v}}{\partial t} = -\nabla\left(p + \frac{2Sv_0}{D}\epsilon_{\parallel}\right) + \left(\nu_0\nabla^2 - \nu_2\nabla^4 + Sv_0\frac{\partial}{\partial x}\right)\delta\mathbf{v} - 2\beta v_0\epsilon_{\parallel}\mathbf{v}_0 \tag{3.16}$$

Once again, considering perturbations of the form $(\delta\mathbf{v}, \delta p) = (\delta\hat{\mathbf{v}}, \delta\hat{p})\exp\left(i\mathbf{k}\cdot\mathbf{r} + \sigma t\right)$ and using the incompressibility condition (3.15), the above equations reduces to the eigenvalue equation

$$\sigma(\mathbf{k})\delta\hat{\mathbf{v}} = -\mathbf{M}\left((\nu_0 k^2 + \nu_2 k^4 - iSk_x v_0)\mathbf{I} - \begin{pmatrix} 2\alpha & 0 \\ 0 & 0 \end{pmatrix}\right)\delta\hat{\mathbf{v}} \tag{3.17}$$

Where $\mathbf{I}$ is the identity matrix and

$$\mathbf{M} = \begin{pmatrix} 1 - \frac{k_x^2}{k^2} & -\frac{k_x k_y}{k^2} \\ -\frac{k_x k_y}{k^2} & 1 - \frac{k_y^2}{k^2} \end{pmatrix}. \tag{3.18}$$

The eigenvalues describing the stability of the polar solution is then given by $\lambda = 0$ and $\lambda = -\left(\nu_0 k^2 + \nu_2 k^4 - iSk_x v_0\right) + 2\alpha k_y^2/k^2$. For $\nu_0 < 0$ and $\nu_2 > 0$ there is once again a region of unstable wavenumbers, where perturbations will exponentially grow as shown in fig 3.4b. For both $\alpha < 0$ and $\nu_0 < 0$ both fixed points are unstable to small wavenumber perturbations implying that (3.6) describes an inhomogeneous velocity field as observed in simulations and pictured in fig 3.5.

To examine the pattern formation properties of (3.6), we will simplify the equation by restricting the analysis to two-dimensional flows in the limit of $S = 0$. From the stability analysis it was found that the S-term was the only term contributing with a complex oscillatory term to the eigenvalue. From simulations it was found that (3.6) has a stable equilibrium state for $S = 0$ given by a square lattice of vortices as shown in fig 3.6a. To examine the stability of the pattern with respect to the other parameters in (3.6), the equation is rewritten as a vector model-A equation

$$\frac{\partial v_i}{\partial t} = -\frac{\delta\mathcal{F}}{\delta v_i}, \tag{3.19}$$

where v_i is the components of $\mathbf{v}$ and the effective free-energy is given by

$$\mathcal{F} = \int dA\left(p\nabla\cdot\mathbf{v} + \frac{1}{2}\left(v_x\mathcal{L}v_x + v_y\mathcal{L}v_y\right) + \frac{\alpha}{2}|\mathbf{v}|^2 + \frac{\beta}{4}|\mathbf{v}|^4\right), \tag{3.20}$$

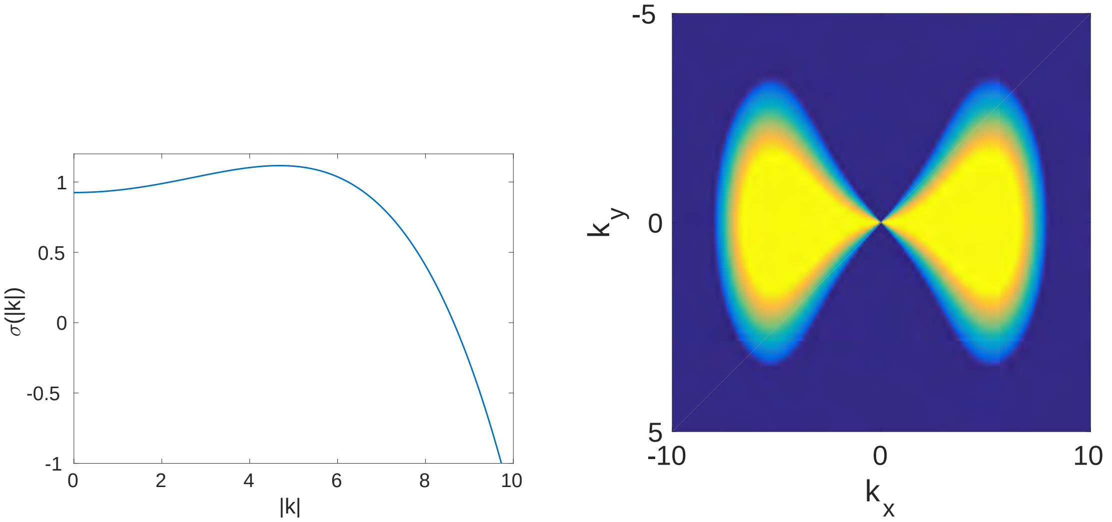

(a) Linear stability region for the $\mathbf{v} = 0$ fixed point. For $\sigma(|k|) > 0$ the fixed point is dynamically unstable.

(b) Linear stability for the fixed point with $\mathbf{v} = \mathbf{v}_0$. The coloured region represents the unstable wavenumbers.

Figure 3.4: Stability regions for the uniform fixed points derived from the linear stability analysis.

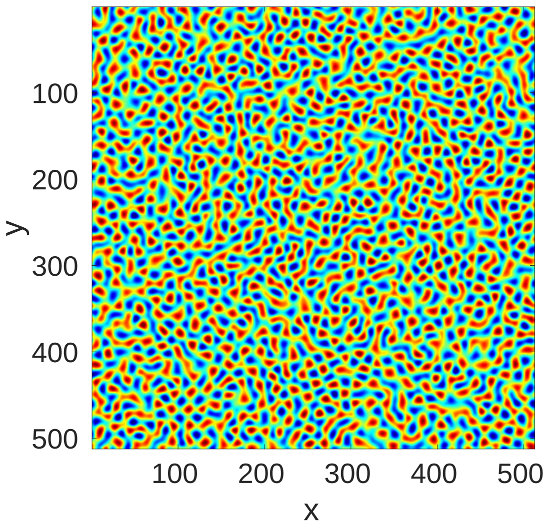

Figure 3.5: Snapshot of the vorticity field of a solution of (3.6). The vorticity peaks move around dynamically in time.

where $\mathcal{L} = -\nu_0 \nabla^2 + \nu_2 \nabla^4$. From (3.20) we find that if v_i is an eigenfunction of $\mathcal{L}$, the energy of the state will only depend on the magnitude of $\mathbf{v}$. In order to asses the stability of the square vorticity pattern, a square and hexagonal vorticity pattern and the uniform velocity solutions are substituted into (3.20) to find their relative stability.

In two dimensions incompressible velocity fields can be formulated as $v_x = \frac{\partial \phi}{\partial y}$ and $v_y = -\frac{\partial \phi}{\partial x}$, which gives $\nabla^2 \phi = \omega$. Furthermore, for incompressible velocity fields the pressure term in (3.20) drops out. The expressions for a square and hexagonal vorticity are given by

$$\omega_s = qA_s\left(\cos(qx) + \cos(qy)\right) \tag{3.21}$$

$$\omega_h = qA_h\left(\cos\left(q\left(\frac{\sqrt{3}}{2}x + \frac{1}{2}y\right)\right) + \cos\left(qy\right) + \cos\left(q\left(\frac{\sqrt{3}}{2}x - \frac{1}{2}y\right)\right)\right). \tag{3.22}$$

When solving the Poisson equation for ϕ, calculating the velocity fields, substituting into (3.20), and averaging over one period we find the energies

$$F_s = \frac{A_s^2}{16}\left(8q^4\nu_2 + 5A_s^2\beta + 8q^2\nu_0 + 8\alpha\right) \tag{3.23}$$

$$F_h = \frac{3A_h^2}{32}\left(8q^4\nu_2 + 9A_h^2\beta + 8q^2\nu_0 + 8\alpha\right) \tag{3.24}$$

$$F_u = -\frac{\alpha^2}{4\beta}, \tag{3.25}$$

where F_u is found by substituting in a uniform velocity field with magnitude $\mathbf{v} = \sqrt{-\alpha/\beta}$. Minimizing the expressions with respect to q and A_i, we find that both patterns have wave number $q_{eq} = \sqrt{|\nu_0|/2\nu_2}$ and the square vorticity lattice is the most stable pattern for all (β, ν_0, ν_2) for $\alpha < 0$. Due to the symmetry of (3.20) the one parameter family consisting of rotations in the velocity plane (v_x, v_y) will generate solutions with equal energy and rotated vorticity pattern. This suggest that (3.6) with $S = 0$ will exhibit different domains with different velocity profiles with grain boundary-like structures in between, as was also found in simulation, shown in fig 3.6b. For $S \neq 0$ the square lattice becomes unstable and we once again find the dynamic state discussed earlier with the mean of $|\mathbf{v}|^2$ dropping from A_s^2 towards zero with increasing S, as shown in fig 3.7.

The effect of cell division on the dynamics of the cell layer was studied experimentally by tracking the motility of cells around a cell division using particle image velocimetry. To get a better signal-to-noise ratio the velocity fields was extracted from an averaged signal using 100 aligned cell divisions.

30 minutes after cell division a distinct vorticity pattern emerges, see fig 3.9a. Adjacent to the division site two primary vortex pairs appear, with a clockwise (red) and a counterclockwise (blue) vortex flanking each daughter cell. These are located approximately one cell diameter away from the division site as shown by the full line in fig 3.9a. Well-ordered secondary and tertiary vortices are also induced by the cell division and appear farther from the division site. At approximately two cell diameters away an ordered ring of eight vortex pairs is observed, the dashed line in fig 3.9a. At a distance of three cell diameters away from the division site another ordered ring of eight vortices emerges, as shown by the dotted line in fig 3.9a. The last vortex pattern is somewhat noisy due to the effects of cell divisions taking place outside the framed region.

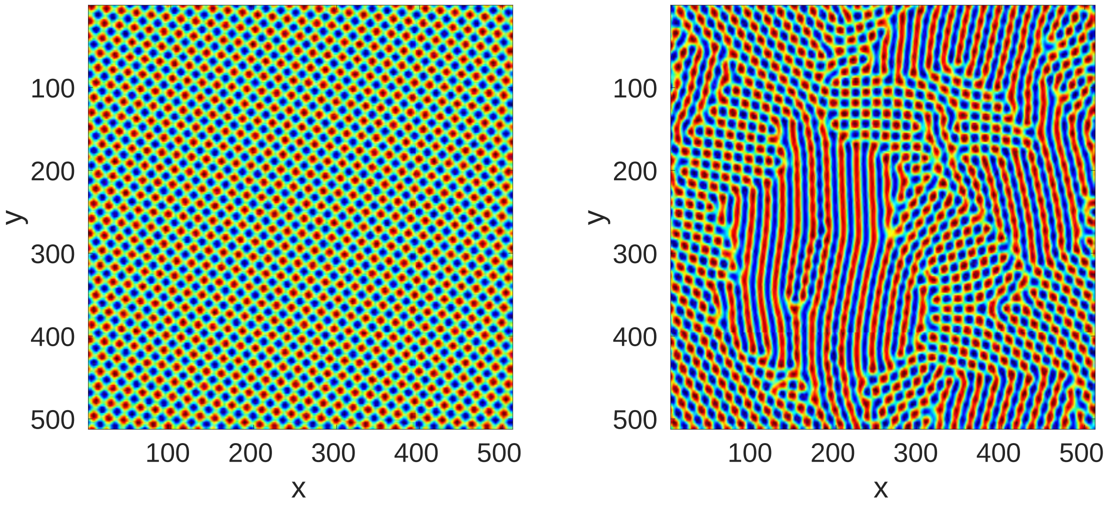

(a) Stable square vorticity pattern generated by (3.6) with $S = 0$.

(b) Snapshot of v_x generated by (3.6) with $S = 0$ showing multiple domains with different velocity profiles describing patches of rotated square vorticity patterns. The domains will coarsen in time towards the stable one domain equilibrium

Figure 3.6: Dynamic and equilibrium properties of (3.6) with $S = 0$

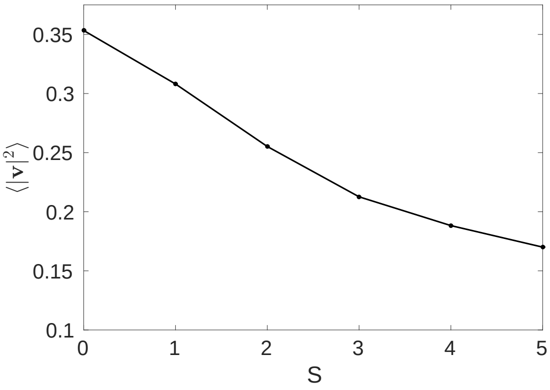

Figure 3.7: The average of $|\mathbf{v}|^2$ as a function of S.

We found that the continuum model in (3.6) reproduces the overall velocity field of a cell layer with a fitted mean velocity given by 1.4μm/min that is close to the experimental velocity of 0.9μm/min as well as reproduces the correct peak velocities and magnitude of the divergence field after cell division. In order to quantify the vorticity patterns from the experiment we performed a Fourier analysis at the bands in 3.9a corresponding to one, two and three cell diameters away from cell division. The same analysis was performed on the simulated cell division vorticity in fig 3.9b. We used the power spectrum of the signals to quantify the emergent patterns at the different lengths which is shown in fig 3.10. Both the experimental and the simulated vorticities show periodic patterns with similar periodicity. Taken together

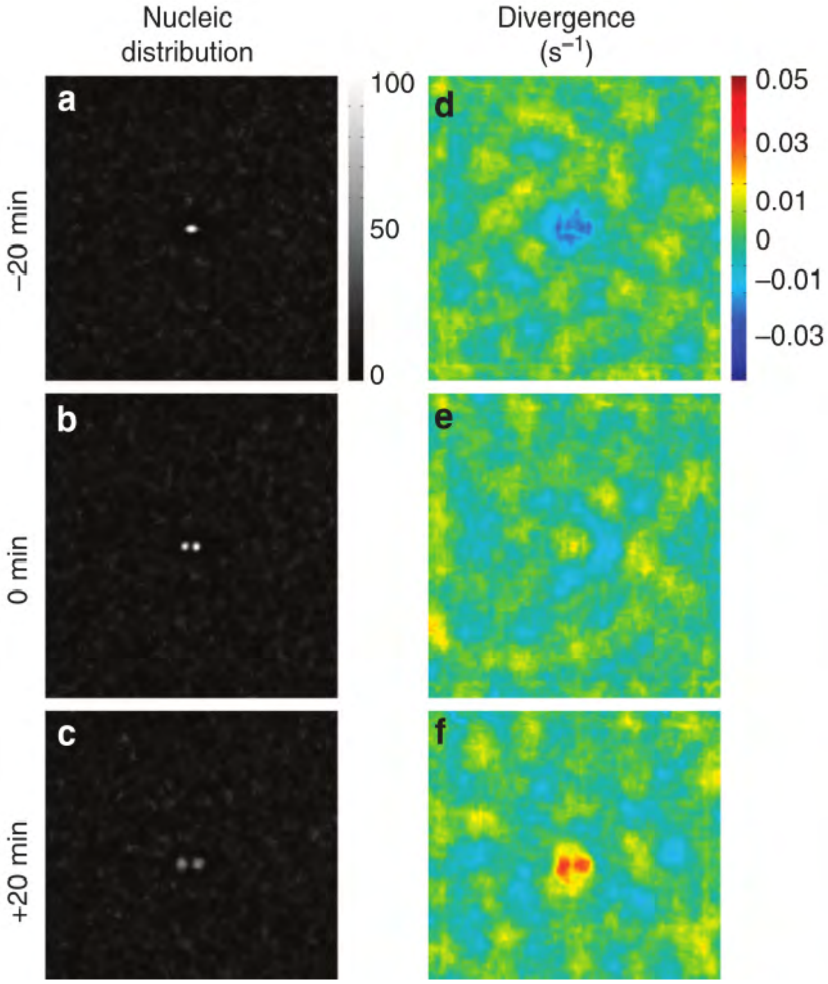

Figure 3.8: Average nuclei positions and divergence of the velocity field around a cell division using 100 cell divisions. $t = 0$ is right after cell division. The left series of pictures is from the phase contrast microscopy while the right series is the calculated divergence field.

with the similar velocity field and peak values, these results implies that the continuum model in (3.6) does capture some of the relevant physics for an active cell layer.

For modelling the hydrodynamics of biological tissue the use of higher order extensions to (3.4) is quite new and the microscopic origin of the negative viscosity term is still an open issue. While similar high-order differential equations for scalar fields can be derived in a variety of ways [8, 15] the generalization to biological systems described by a vector field is not obvious. For some types of flow it can be shown that local perturbations can lead to negative viscosities [82], but often the initial flow has to be periodic or simple in some other sense. Recently, a microscopic model for a self-propelled particles with short-ranged alignment and long-range anti-alignment has been shown to generate a negative viscosity term in the continuum limit [83]. This suggests that a full microscopic derivation of (3.6) can soon be developed.

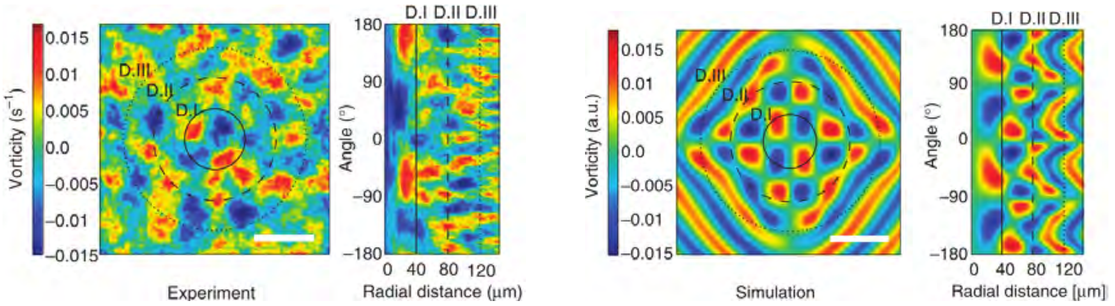

(a) The experimental vorticity field emerging 30 minutes after cell division. The left picture is the vorticity in Cartesian coordinates. The right picture is the vorticity in polar coordinates. Images are the result of averaging over 100 cell divisions. The full, dashed and dotted line denoted D.I, D.II and D.III are one, two and three cell diameters from the centre corresponding to 40, 80 and 120 μm.

(b) Vorticity pattern arising from the numerical simulation of (3.6). The left picture is the vorticity in Cartesian coordinates. The right picture is the vorticity in polar coordinates. The full, dashed and dotted lines are analogous of the lines in the experimental vorticity.

Figure 3.9: Comparison of the vorticity pattern induced by a cell division ina a experimentally set-up and in the continuum model equation (3.6).

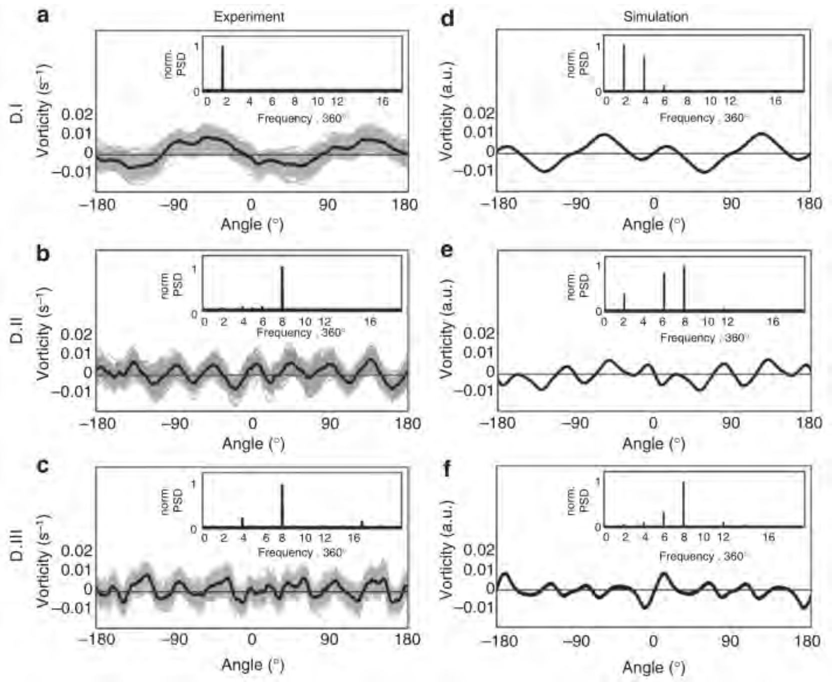

Figure 3.10: Quantification of primary, secondary and tertiary induced vortices. On the left side are the averaged measured vorticity patterns after 30 minutes in polar coordinates at one, two and three cell diameters obtained in experiment. The solid line is the averaged vorticity signal of the gray lines. The inset is the power spectrum of the signal used to quantify the pattern. To the right side are the simulated counter parts.

CHAPTER 4

Conclusion

In this thesis we have studied two models for pattern formations used in describing passive and active matter systems.

The phase field crystal model has been introduced and shown to qualitatively describe equilibrium properties of crystalline materials. The simplest form of the equation of motion is an overdamped diffusion equation, which has been used to study the coarsening dynamics of two and three dimensional polycrystalline structures [50, 56].

In two dimensions it was found that the coarsening dynamics is highly dependent on the quenching temperature, grain rotation, and complex interaction between neighbouring grains, resulting in a large spread in coarsening exponents terminating in a stagnating regime, where the coarsening dynamics stops all together. For individual grains it was found that the ratio of rotation and growth followed robust power law statistics independent on quenching temperature.

In three dimensions similar dynamics was observed with an added exponential coarsening regime due to rapid rotation of smaller crystals. The coarsening dynamics was furthermore driven by anomalous growth, where a few grains grow faster than the rest of the crystal matrix.

To study plastic deformations a modified phase field crystal model has been introduced, which generalizes the dynamical equation into a damped wave equation, thus introducing a faster time scale for elastic relaxation of the density field. The modified equation was used to study the fluctuating dislocation number density in a continuously sheared crystal [66]. It was found that the power spectrum of the fluctuating signal follows a power law, while the probability density function evolves from a bimodal function to a unimodal function with the strain rate. It was showed that both the power spectrum and functional form of the probability density could be described by a solution to a Langevin equation for the density of dislocations.

To study the dynamics of an endothelial cell layer, a hydrodynamical vector model has been introduced, which could be seen as a generalization of the scalar field theory used in describing crystals. It was shown that it could describe the long range ordered vorticity patterns observed in cell division in an endothelial cell layer [5], and that a simplified version could be formulated as a vector model-A theory from which the amplitude of the equilibrium square pattern could be derived.

While higher order hydrodynamical models can be used to describe mesoscopic low Reynolds number turbulence and give rise to a characteristic vorticity length scale, it is a problem that no clear microscopic derivation exists. It is also an open question how to generalize these models to other symmetries besides square lattices. Taking inspiration from the scalar phase field crystal model [84, 85], other lattice structures such as hexagonal might be possible by generalizing the linear differential operator to higher orders which, however, will probably only complicate the task of performing a microscopic derivation.

Appendix A

Static Properties of the Phase Field Crystal Model

A.1 The phase field crystal phase diagram

In order to calculate the phase diagram we need to calculate the energy densities for the relevant phases, which in 3 dimensions are planes, hexagonal rods and body-centered cubic and use the equal tangent construction to find the coexistence regions and transition lines. The phase field crystal free energy is given by

$$\mathcal{F} = \int dV \left(\frac{1}{2}\phi \left(\nabla^2 + 1\right)^2 \phi + \frac{\epsilon}{2}\phi^2 + \frac{1}{4}\phi^4 \right). \tag{A.1}$$

In general the density field can be expanded as

$$\phi = \phi_0 + \sum_{\mathbf{G}} A_{\mathbf{G}} \exp\left(\mathrm{i}\mathbf{G}\cdot\mathbf{r}\right) + \text{c.c}, \tag{A.2}$$

where $\mathbf{G}_i$ are reciprocal lattice vectors. Due to mass conservation and in order to derive the coexistence regions it is necessary to keep the constant mean density ϕ_0 in the expansion. Because of the one mode dominance of (A.1) the sum will be truncated using the set of smallest lattice vectors corresponding to the lattice.

The density expansion for planes is simply

$$\phi = \phi_0 + A_1 \cos(qx). \tag{A.3}$$

Substituting into (A.1) and integrating over 1 period we find

$$F(q, A_1, \phi_0) = \frac{3}{32}A_1^4 + \left(\frac{1}{4}q^4 + \frac{3}{4}\phi_0^2 - \frac{1}{2}q^2 + \frac{1}{4}\epsilon + \frac{1}{4}\right)A_1^2 + \frac{1}{4}\phi_0^4 + \frac{1}{2}\epsilon\phi_0^4. \tag{A.4}$$

Minimizing with respect to q and A_1 we find the equilibrium expressions

$$q_{eq} = 1 \tag{A.5}$$

$$A_1^{eq} = \frac{2}{3}\sqrt{-9\phi_0^2 - 3\epsilon}. \tag{A.6}$$

The density expansion for hexagonal rods to lowest order is given by

$$\phi = \phi_0 + A_2 \left(\frac{1}{2} \cos\left(\frac{2qy}{\sqrt{3}}\right) - \cos\left(qx\right) \cos\left(\frac{qy}{\sqrt{3}}\right) \right). \tag{A.7}$$

Inserting into (A.1), integrating over 1 unit cell and minimizing with respect to q and A_2 we find

$$\begin{aligned} F(q, A_2, \phi_0) =& \frac{45}{512} A_2^4 - \frac{3}{16} A_2^3 \phi_0 + \left(\frac{1}{3} q^4 + \frac{9}{16} \phi_0^2 - \frac{1}{2} q^2 + \frac{3}{16} (\epsilon + 1) \right) A_2^2 \\ & + \frac{1}{4} \phi_0^4 + \frac{1}{2} (\epsilon + 1) \phi_0^2 & \text{(A.8)} \\ q_{eq} =& \frac{\sqrt{3}}{2} & \text{(A.9)} \\ A_2^{eq} =& \frac{4}{5} \phi_0 + \frac{4}{15} \sqrt{-36\phi^2 - 15\epsilon}. & \text{(A.10)} \end{aligned}$$

The density expansion for a body-centered cubic lattice to lowest order is given by

$$\phi = \phi_0 + A_3 \left(\cos\left(qx\right) \cos\left(qy\right) + \cos\left(qx\right) \cos\left(qz\right) + \cos\left(qy\right) \cos\left(qz\right) \right). \tag{A.11}$$

Inserting into (A.1), integrating over 1 unit cell and minimizing with respect to q and A_3 we find the last energy is given by

$$\begin{aligned} F(q, A_3, \phi_0) =& \frac{135}{256} A_3^4 + \frac{3}{4} A_3^3 \phi_0 + \left(\frac{2}{3} q^4 + \frac{9}{8} \phi_0^2 - \frac{3}{2} q^2 \frac{3}{8} (\epsilon + 1) \right) A_3^2 \\ & + \frac{1}{4} \phi_0^4 + \frac{1}{2} (\epsilon + 1) \phi_0^2 & \text{(A.12)} \\ q_{eq} =& \frac{1}{\sqrt{2}} & \text{(A.13)} \\ A_3^{eq} =& -\frac{8}{15} \phi_0 + \frac{4}{15} \sqrt{-11\phi_0^2 - 5\epsilon}. & \text{(A.14)} \end{aligned}$$

The free energy for the uniform liquid state is simply given by

$$F = \frac{1}{4} \phi_0^4 + \frac{1}{2} (\epsilon + 1) \phi_0^2. \tag{A.15}$$

The Maxwell common tangent is constructed by numerically solving the 2 coupled equations for fixed ϵ

$$\frac{\partial F_i}{\partial \phi_0} = \frac{\partial F_j}{\partial \phi_0} \tag{A.16}$$

$$F_i - \frac{\partial F_i}{\partial \phi_0} \phi_0 = F_j - \frac{\partial F_j}{\partial \phi_0} \phi_0, \tag{A.17}$$

from which we can draw the phase diagram in fig A.1b.

A.2 Stress-strain curve for area preserving strain in 2 dimensions

The 2 dimensional density with hexagonal symmetry is expanded as

$$\phi = \phi_0 + A_2 \left(\frac{1}{2} \cos\left(\frac{2q_y y}{\sqrt{3}}\right) - \cos\left(q_x x\right) \cos\left(\frac{q_y y}{\sqrt{3}}\right) \right). \tag{A.18}$$

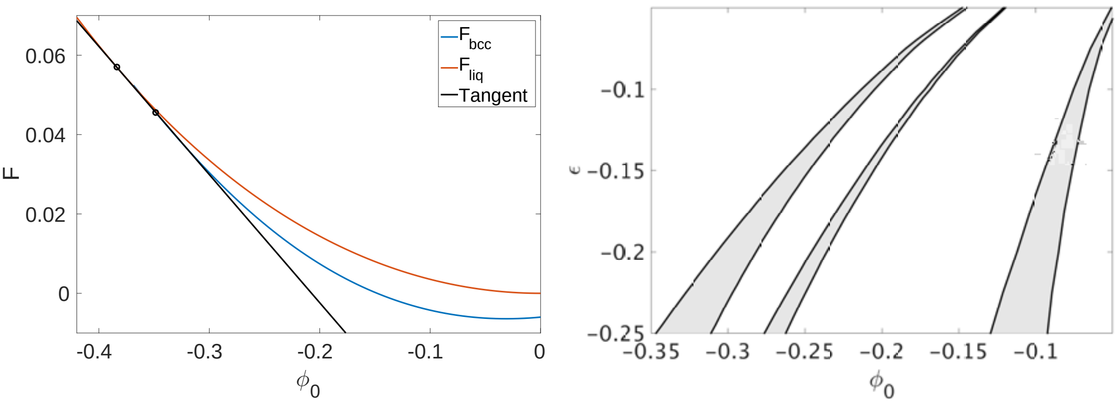

(a) The free-energy of the liquid and body-centered cubic lattice and their common tangent.

(b) The phase diagram found using the common tangent construction.

Figure A.1: The phase field crystal phase diagram.

Inserting into (A.1), integrating over 1 unit cell and minimizing with respect to A_2 to find the free energy $F(q_x, q_y, A_2, \phi_0)$. Using $q_x = 1 + \delta$, $q_y = 1/(1+\delta)$ and $\frac{\partial F}{\partial \delta} = \sigma$ we can find the stress strain curve.

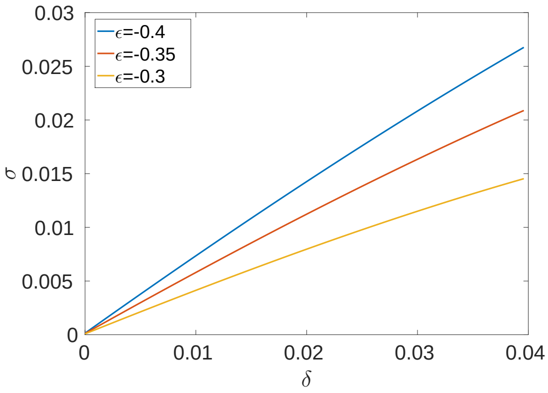

Figure A.2: Stress-strain curve for a 2 dimensional hexagonal lattice under area preserving strain. For small strains the curve is linear as predicted by the long wave length approximation discussed in the phase field crystal chapter.

Appendix B

Integration schemes

B.1 The Phase Field Crystal Model.

The overdamped equations of motion for the phase field crystal model

$$\frac{\partial \phi}{\partial t} = L\phi + \nabla^2 \phi^3, \tag{B.1}$$

where $L = \nabla^2 \left(\left(1+\nabla^2\right)^2 + \epsilon \right)$ has been solved using an explicit exponential time integration scheme in Fourier space given by[86],

$$\hat{\phi}_{n+1} = \exp(\hat{L}dt)\hat{\phi}_n - \frac{k^2}{\hat{L}} \left(\exp(\hat{L}dt) - 1\right) \hat{\phi_n}^3, \tag{B.2}$$

where hats denotes Fourier transformed quantities and k is the magnitude of the wavenumber vector $\mathbf{k}$. The non-linear term was evaluated by transforming back to real space, performing the exponentiation and transforming back to Fourier space. To suppress aliasing errors we used a 2/3-rule.

In order to solve the modified phase field crystal model the equation was rewritten as

$$\frac{\partial \mathbf{b}}{\partial t} = \mathbf{M}\mathbf{b} + \mathbf{f}, \tag{B.3}$$

where we have defined

$$\mathbf{b} = \begin{pmatrix} \phi \\ \partial_t \phi \end{pmatrix}, \quad \mathbf{M} = \begin{pmatrix} 0 & 1 \\ \alpha^2 \nabla^2 \left(\left(1+\nabla^2\right)^2 + \epsilon \right) & -\beta \end{pmatrix} \quad \text{and} \quad \mathbf{f} = \begin{pmatrix} 0 \\ \alpha^2 \nabla^2 \phi \end{pmatrix}. \tag{B.4}$$

Due to stability issues the equations of motion was solved by an semi implicit exponential integration scheme with the update equations given by [86, 87]

$$\hat{\mathbf{b}}_{n+1} = \exp(\mathbf{M}dt)\hat{\mathbf{b}}_n + \mathbf{M}^{-1}\left(\exp(\mathbf{M}dt) - \mathbf{I}\right)\hat{\mathbf{f}}_n + \mathbf{M}^{-2}\left(\exp(\mathbf{M}dt) - \mathbf{I} - \mathbf{M}dt\right)\left(\hat{\mathbf{f}}_{n+1} - \hat{\mathbf{f}}_n\right), \tag{B.5}$$

where $\mathbf{I}$ is the identity matrix and $\hat{\mathbf{f}}_{n+1}$ is approximated by the solution of (B.5) without the $\mathbf{M}^{-2}$ term.

B.2 Vector Model for Active Matter

The vector model for active matter is given by

$$\frac{\partial \mathbf{v}}{\partial t} = -\frac{1}{\rho}\nabla p + \frac{S}{\rho}\left(\mathbf{v}\cdot\nabla\right)\mathbf{v} - \frac{S}{\rho D}\nabla|\mathbf{v}|^2 + \nu_0\nabla^2\mathbf{v} - \nu_2\nabla^4 - \left(\alpha + \beta|\mathbf{v}|^2\right)\mathbf{v} \tag{B.6}$$

$$\nabla\cdot\mathbf{v} = 0. \tag{B.7}$$

Taking the divergence of (B.6) and using the incompressibility condition we find the Poisson equation for the pressure

$$\nabla^2 p = \frac{S}{\rho}\left(\nabla v_x\cdot\partial_x\mathbf{v} + \nabla v_y\cdot\partial_y\mathbf{v}\right) - \frac{S}{\rho D}\nabla^2|\mathbf{v}|^2 - \beta\mathbf{v}\cdot\nabla|\mathbf{v}|^2. \tag{B.8}$$

To keep the velocity field divergence free the Poisson equation is modified with an divergence damping term to [88]

$$\nabla^2 p = \frac{S}{\rho}\left(\nabla v_x\cdot\partial_x\mathbf{v} + \nabla v_y\cdot\partial_y\mathbf{v}\right) - \frac{S}{\rho D}\nabla^2|\mathbf{v}|^2 - \beta\mathbf{v}\cdot\nabla|\mathbf{v}|^2 + \zeta\nabla\cdot\mathbf{v}. \tag{B.9}$$

To see why this dampens the divergence of the velocity field, once again take the divergence of (B.6) to get

$$\frac{\partial \delta}{\partial t} = \frac{S}{\rho}\left(\mathbf{v}\cdot\nabla\right)\delta + \nu_0\nabla^2\delta - \nu_2\nabla^4\delta - \left(\alpha + \beta|\mathbf{v}|^2 + \zeta\right)\delta, \tag{B.10}$$

where $\delta = \nabla\cdot\mathbf{v}$. For sufficiently large ζ the last term will be a linear damping term exponentially damping δ.

The velocity equation (B.6) was solved in Fourier space using the explicit exponential time integration scheme in (B.2) with the pressure equation solved in Fourier space. All non-linear terms was evaluated in real space and transformed back.

The scheme has been tested for a wide range of parameters and was found to generate average and peak values of δ far below the numerical truncation errors of the update scheme.

Bibliography

[1] Flock of birds. `http://darkroom.baltimoresun.com/wp-content/uploads/2014/02/AFP_Getty-526984630.jpg`. Accessed: 2015-08-06.

[2] Luis H Cisneros, Ricardo Cortez, Christopher Dombrowski, Raymond E Goldstein, and John O Kessler. Fluid dynamics of self-propelled microorganisms, from individuals to concentrated populations. *Experiments in Fluids*, 43(5):737–753, 2007.

[3] John Toner and Yuhai Tu. Flocks, herds, and schools: A quantitative theory of flocking. *Physical review E*, 58(4):4828, 1998.

[4] Henricus H Wensink, Jörn Dunkel, Sebastian Heidenreich, Knut Drescher, Raymond E Goldstein, Hartmut Löwen, and Julia M Yeomans. Meso-scale turbulence in living fluids. *Proceedings of the National Academy of Sciences*, 109(36):14308–14313, 2012.

[5] Ninna S Rossen, Jens M Tarp, Joachim Mathiesen, Mogens H Jensen, and Lene B Oddershede. Long-range ordered vorticity patterns in living tissue induced by cell division. *Nature communications*, 5, 2014.

[6] Mark C Cross and Pierre C Hohenberg. Pattern formation outside of equilibrium. *Reviews of modern physics*, 65(3):851, 1993.

[7] A Jaatinen and T Ala-Nissila. Extended phase diagram of the three-dimensional phase field crystal model. *Journal of Physics: Condensed Matter*, 22(20):205402, 2010.

[8] J Swift and Pierre C Hohenberg. Hydrodynamic fluctuations at the convective instability. *Physical Review A*, 15(1):319, 1977.

[9] Nikolas Provatas and Ken Elder. *Phase-field methods in materials science and engineering*. John Wiley & Sons, 2011.

[10] Gian-Luca Oppo, Giampaolo Dâ^{TM}Alessandro, and William J Firth. Spatiotemporal instabilities of lasers in models reduced via center manifold techniques. *Physical Review A*, 44(7):4712, 1991.

[11] Norbert Stoop, Romain Lagrange, Denis Terwagne, Pedro M Reis, and Jörn Dunkel. Curvature-induced symmetry breaking determines elastic surface patterns. *Nature materials*, 2015.

[12] Pierre C Hohenberg and Bertrand I Halperin. Theory of dynamic critical phenomena. *Reviews of Modern Physics*, 49(3):435, 1977.

[13] KR Elder and Martin Grant. Modeling elastic and plastic deformations in nonequilibrium processing using phase field crystals. *Physical Review E*, 70(5):051605, 2004.

[14] BN Belintsev, MA Livshits, and MV Volkenstein. Pattern formation in systems with nonlocal interactions. *Zeitschrift für Physik B Condensed Matter*, 44(4):345–351, 1981.

[15] Yoshiki Kuramoto and Toshio Tsuzuki. On the formation of dissipative structures in reaction-diffusion systems reductive perturbation approach. *Progress of Theoretical Physics*, 54(3):687–699, 1975.

[16] GI Sivashinsky. Nonlinear analysis of hydrodynamic instability in laminar flamesâ"i. derivation of basic equations. *Acta astronautica*, 4(11):1177–1206, 1977.

[17] DT Papageorgiou, C Maldarelli, and DS Rumschitzki. Nonlinear interfacial stability of core-annular film flows. *Physics of Fluids A: Fluid Dynamics (1989-1993)*, 2(3):340–352, 1990.

[18] Rodolfo Cuerno and Albert-László Barabási. Dynamic scaling of ion-sputtered surfaces. *Physical review letters*, 74(23):4746, 1995.

[19] Basil Nicolaenko, Bruno Scheurer, and Roger Temam. Some global dynamical properties of the kuramoto-sivashinsky equations: Nonlinear stability and attractors. *Physica D: Nonlinear Phenomena*, 16(2):155–183, 1985.

[20] Kim Sneppen, J Krug, MH Jensen, C Jayaprakash, and T Bohr. Dynamic scaling and crossover analysis for the kuramoto-sivashinsky equation. *Physical Review A*, 46(12):R7351, 1992.

[21] SA Brazovskii. Phase transition of an isotropic system to a nonuniform state. *WORLD SCIENTIFIC SERIES IN 20TH CENTURY PHYSICS*, 11:109–113, 1995.

[22] Alain Karma and Wouter-Jan Rappel. Quantitative phase-field modeling of dendritic growth in two and three dimensions. *Physical review E*, 57(4):4323, 1998.

[23] R Folch, J Casademunt, A Hernández-Machado, and L Ramirez-Piscina. Phase-field model for hele-shaw flows with arbitrary viscosity contrast. i. theoretical approach. *Physical Review E*, 60(2):1724, 1999.

[24] John W Cahn and John E Hilliard. Free energy of a nonuniform system. iii. nucleation in a two-component incompressible fluid. *The Journal of chemical physics*, 31(3):688–699, 1959.

[25] JS Langer. Instabilities and pattern formation in crystal growth. *Reviews of Modern Physics*, 52(1):1, 1980.

[26] G Caginalp. Stefan and hele-shaw type models as asymptotic limits of the phase-field equations. *Physical Review A*, 39(11):5887, 1989.

[27] Robert V Kohn and Felix Otto. Upper bounds on coarsening rates. *Communications in mathematical physics*, 229(3):375–395, 2002.

[28] Heike Emmerich. *The diffuse interface approach in materials science: thermodynamic concepts and applications of phase-field models*, volume 73. Springer Science & Business Media, 2003.

[29] KR Elder, Mark Katakowski, Mikko Haataja, and Martin Grant. Modeling elasticity in crystal growth. *Physical review letters*, 88(24):245701, 2002.

[30] David Jasnow. Critical phenomena at interfaces. *Reports on Progress in Physics*, 47:1059–1132, 1984.

[31] KR Elder, Martin Grant, Nikolas Provatas, and JM Kosterlitz. Sharp interface limits of phase-field models. *Physical Review E*, 64(2):021604, 2001.

[32] Alain Karma and Wouter-Jan Rappel. Phase-field method for computationally efficient modeling of solidification with arbitrary interface kinetics. *Physical Review E*, 53(4):R3017, 1996.

[33] Mikko Haataja, Judith Müller, AD Rutenberg, and Martin Grant. Dislocations and morphological instabilities: Continuum modeling of misfitting heteroepitaxial films. *Physical Review B*, 65(16):165414, 2002.

[34] Dong-Hee Yeon, Pil-Ryung Cha, Ji-Hee Kim, Martin Grant, and Jong-Kyu Yoon. A phase field model for phase transformation in an elastically stressed binary alloy. *Modelling and Simulation in Materials Science and Engineering*, 13(3):299, 2005.

[35] KR Elder, Nikolas Provatas, Joel Berry, Peter Stefanovic, and Martin Grant. Phase-field crystal modeling and classical density functional theory of freezing. *Physical Review B*, 75(6):064107, 2007.

[36] Dong-Hee Yeon, Zhi-Feng Huang, KR Elder, and K Thornton. Density-amplitude formulation of the phase-field crystal model for two-phase coexistence in two and three dimensions. *Philosophical Magazine*, 90(1-4):237–263, 2010.

[37] Paul M Chaikin and Tom C Lubensky. *Principles of condensed matter physics*, volume 1. Cambridge Univ Press, 2000.

[38] Pak Yuen Chan and Nigel Goldenfeld. Nonlinear elasticity of the phase-field crystal model from the renormalization group. *Physical Review E*, 80(6):065105, 2009.

[39] Gyula I Tóth and Nikolas Provatas. Advanced ginzburg-landau theory of freezing: A density-functional approach. *Physical Review B*, 90(10):104101, 2014.

[40] A Jaatinen, CV Achim, KR Elder, and T Ala-Nissila. Thermodynamics of bcc metals in phase-field-crystal models. *Physical Review E*, 80(3):031602, 2009.

[41] Peter Stefanovic, Mikko Haataja, and Nikolas Provatas. Phase field crystal study of deformation and plasticity in nanocrystalline materials. *Physical Review E*, 80(4):046107, 2009.

[42] Adrian P Sutton and Robert W Balluffi. Interfaces in crystalline materials. 1995.

[43] Yu Mishin, M Asta, and Ju Li. Atomistic modeling of interfaces and their impact on microstructure and properties. *Acta Materialia*, 58(4):1117–1151, 2010.

[44] William W Mullins. Two-dimensional motion of idealized grain boundaries. *Journal of Applied Physics*, 27(8):900–904, 1956.

[45] Sascha Hilgenfeldt, Andrew M. Kraynik, Stephan A. Koehler, and Howard A. Stone. An accurate von neumann's law for three-dimensional foams. *Physical Review Letters*, 86(12):2685–2688, 2001.

[46] Robert D MacPherson and David J Srolovitz. The von neumann relation generalized to coarsening of three-dimensional microstructures. *Nature*, 446(7139):1053–1055, 2007.

[47] KR Elder, Jorge Viñals, and Martin Grant. Ordering dynamics in the two-dimensional stochastic swift-hohenberg equation. *Physical review letters*, 68(20):3024, 1992.

[48] MC Cross and DI Meiron. Domain coarsening in systems far from equilibrium. *Physical review letters*, 75(11):2152, 1995.

[49] Jacob J Christensen and Alan J Bray. Pattern dynamics of rayleigh-bénard convective rolls and weakly segregated diblock copolymers. *Physical Review E*, 58(5):5364, 1998.

[50] Mathias Bjerre, Jens M Tarp, Luiza Angheluta, and Joachim Mathiesen. Rotation-induced grain growth and stagnation in phase-field crystal models. *Physical Review E*, 88(2):020401, 2013.

[51] R Backofen, K Barmak, KE Elder, and A Voigt. Capturing the complex physics behind universal grain size distributions in thin metallic films. *Acta Materialia*, 64:72–77, 2014.

[52] Elizabeth A Holm and Stephen M Foiles. How grain growth stops: A mechanism for grain-growth stagnation in pure materials. *Science*, 328(5982):1138–1141, 2010.

[53] John W Cahn and Jean E Taylor. A unified approach to motion of grain boundaries, relative tangential translation along grain boundaries, and grain rotation. *Acta materialia*, 52(16):4887–4898, 2004.

[54] Hsun Hu and BB Rath. On the time exponent in isothermal grain growth. *Metallurgical Transactions*, 1(11):3181–3184, 1970.

[55] KE Harris, VV Singh, and AH King. Grain rotation in thin films of gold. *Acta materialia*, 46(8):2623–2633, 1998.

[56] Jens M. Tarp and Joachim Mathiesen. Rotation-limited growth of three-dimensional body-centered-cubic crystals. *Phys. Rev. E*, 92:012409, Jul 2015.

[57] Péter Dusán Ispánovity, István Groma, Wolfgang Hoffelner, and Maria Samaras. Abnormal subgrain growth in a dislocation-based model of recovery. *Modelling and Simulation in Materials Science and Engineering*, 19(4):045008, 2011.

[58] M Ferry and FJ Humphreys. Discontinuous subgrain growth in deformed and annealed $\{110\}< 001>$ aluminium single crystals. *Acta materialia*, 44(4):1293–1308, 1996.

[59] Ari Adland, Yechuan Xu, and Alain Karma. Unified theoretical framework for polycrystalline pattern evolution. *Physical review letters*, 110(26):265504, 2013.

[60] Jerome Weiss and Jean-Robert Grasso. Acoustic emission in single crystals of ice. *The Journal of Physical Chemistry B*, 101(32):6113–6117, 1997.

[61] Thiebaud Richeton, Jérôme Weiss, and François Louchet. Dislocation avalanches: role of temperature, grain size and strain hardening. *Acta materialia*, 53(16):4463–4471, 2005.

[62] Peter Stefanovic, Mikko Haataja, and Nikolas Provatas. Phase-field crystals with elastic interactions. *Physical review letters*, 96(22):225504, 2006.

[63] Pak Yuen Chan, Georgios Tsekenis, Jonathan Dantzig, Karin A Dahmen, and Nigel Goldenfeld. Plasticity and dislocation dynamics in a phase field crystal model. *Physical review letters*, 105(1):015502, 2010.

[64] Thiebaud Richeton, Patrik Dobron, Frantisek Chmelik, Jérôme Weiss, and Francois Louchet. On the critical character of plasticity in metallic single crystals. *Materials Science and Engineering: A*, 424(1):190–195, 2006.

[65] Dennis M Dimiduk, Chris Woodward, Richard LeSar, and Michael D Uchic. Scale-free intermittent flow in crystal plasticity. *Science*, 312(5777):1188–1190, 2006.

[66] Jens M Tarp, Luiza Angheluta, Joachim Mathiesen, and Nigel Goldenfeld. Intermittent dislocation density fluctuations in crystal plasticity from a phase-field crystal model. *Physical review letters*, 113(26):265503, 2014.

[67] B Caroli, C Caroli, and B Roulet. High-frequency power spectra of systems described by non-linear langevin equations. *Physica A: Statistical Mechanics and its Applications*, 112(3):517–522, 1982.

[68] JJ Brey, JM Casado, and M Morillo. Spectral density from nonlinear fokker-planck equations: The high-frequency limit. *Physical Review A*, 30(3):1535, 1984.

[69] D Sigeti and W Horsthemke. High-frequency power spectra for systems subject to noise. *Physical Review A*, 35(5):2276, 1987.

[70] Tamás Vicsek, András Czirók, Eshel Ben-Jacob, Inon Cohen, and Ofer Shochet. Novel type of phase transition in a system of self-driven particles. *Physical review letters*, 75(6):1226, 1995.

[71] Jerome Buhl, David JT Sumpter, Iain D Couzin, Joe J Hale, Emma Despland, ER Miller, and Steve J Simpson. From disorder to order in marching locusts. *Science*, 312(5778):1402–1406, 2006.

[72] Kunal Bhattacharya and Tamás Vicsek. Collective decision making in cohesive flocks. *New Journal of Physics*, 12(9):093019, 2010.

[73] Saverio E Spagnolie and Eric Lauga. Hydrodynamics of self-propulsion near a boundary: predictions and accuracy of far-field approximations. *Journal of Fluid Mechanics*, 700:105–147, 2012.

[74] TJ Pedley. Instability of uniform micro-organism suspensions revisited. *Journal of Fluid Mechanics*, 647:335–359, 2010.

[75] John Toner, Yuhai Tu, and Sriram Ramaswamy. Hydrodynamics and phases of flocks. *Annals of Physics*, 318(1):170–244, 2005.

[76] Andrey Sokolov and Igor S Aranson. Physical properties of collective motion in suspensions of bacteria. *Physical review letters*, 109(24):248109, 2012.

[77] Uriel Frisch. *Turbulence: the legacy of AN Kolmogorov*. Cambridge university press, 1995.

[78] Xavier Trepat, Michael R Wasserman, Thomas E Angelini, Emil Millet, David A Weitz, James P Butler, and Jeffrey J Fredberg. Physical forces during collective cell migration. *Nature physics*, 5(6):426–430, 2009.

[79] Dhananjay T Tambe, C Corey Hardin, Thomas E Angelini, Kavitha Rajendran, Chan Young Park, Xavier Serra-Picamal, Enhua H Zhou, Muhammad H Zaman, James P Butler, David A Weitz, et al. Collective cell guidance by cooperative intercellular forces. *Nature materials*, 10(6):469–475, 2011.

[80] Jae Hun Kim, Xavier Serra-Picamal, Dhananjay T Tambe, Enhua H Zhou, Chan Young Park, Monirosadat Sadati, Jin-Ah Park, Ramaswamy Krishnan, Bomi Gweon, Emil Millet, et al. Propulsion and navigation within the advancing monolayer sheet. *Nature materials*, 12(9):856–863, 2013.

[81] J Prost. *The physics of liquid crystals*. Number 83. Oxford university press, 1995.

[82] S Gama, M Vergassola, and U Frisch. Negative eddy viscosity in isotropically forced two-dimensional flow: linear and nonlinear dynamics. *J. Fluid Mech*, 260:95–126, 1994.

[83] Robert Großmann, Pawel Romanczuk, Markus Bär, and Lutz Schimansky-Geier. Vortex arrays and mesoscale turbulence of self-propelled particles. *Physical review letters*, 113(25):258104, 2014.

[84] Kuo-An Wu, Ari Adland, and Alain Karma. Phase-field-crystal model for fcc ordering. *Physical Review E*, 81(6):061601, 2010.

[85] Michael Greenwood, Nikolas Provatas, and Jörg Rottler. Free energy functionals for efficient phase field crystal modeling of structural phase transformations. *Physical review letters*, 105(4):045702, 2010.

[86] SM Cox and PC Matthews. Exponential time differencing for stiff systems. *Journal of Computational Physics*, 176(2):430–455, 2002.

[87] MC Cross, D Meiron, and Yuhai Tu. Chaotic domains: A numerical investigation. *Chaos: An Interdisciplinary Journal of Nonlinear Science*, 4(4):607–619, 1994.

[88] WD Henshaw and NA Petersson. A split-step scheme for the incompressible navier-stokes equations. 2001.